Available online at www.sciencedirect.com
SCIENCE DIRECT®
Journal of Computational Physics 214 (2006) 12–40
JOURNAL OF COMPUTATIONAL PHYSICS
www.elsevier.com/locate/jcp

Spatial discretizations for self-adjoint forms of the radiative transfer equations

Jim E. Morel [a,*], B. Todd Adams [b], Taewan Noh [b,c], John M. McGhee [d], Thomas M. Evans [b], Todd J. Urbatsch [b]

[a] Texas A&M University, Department of Nuclear Engineering, 129 Zachry Engineering Center, College Station, TX 77843-3133, United States
[b] Computer and Computational Sciences Division, Los Alamos National Laboratory, Los Alamos, NM 87545, United States
[c] Department of Mathematics, Hongik University, Seoul, South Korea
[d] Transpire Technologies, 6659 Kimball Drive, Suite D-404, Gig Harbor, Washington 98335, United States

Received 2 March 2005; received in revised form 16 August 2005; accepted 6 September 2005
Available online 9 November 2005

Abstract

There are three commonly recognized second-order self-adjoint forms of the neutron transport equation: the even-parity equations, the odd-parity equations, and the self-adjoint angular flux equations. Because all of these equations contain second-order spatial derivatives and are self-adjoint for the mono-energetic case, standard continuous finite-element discretization techniques have proved quite effective when applied to the spatial variables. We first derive analogs of these equations for the case of time-dependent radiative transfer. The primary unknowns for these equations are functions of the angular intensity rather than the angular flux, hence the analog of the self-adjoint angular flux equation is referred to as the self-adjoint angular intensity equation. Then we describe a general, arbitrary-order, continuous spatial finite-element approach that is applied to each of the three equations in conjunction with backward-Euler differencing in time. We refer to it as the "standard" technique. We also introduce an alternative spatial discretization scheme for the self-adjoint angular intensity equation that requires far fewer unknowns than the standard method, but appears to give comparable accuracy. Computational results are given that demonstrate the validity of both of these discretization schemes.

Keywords: Thermal radiation transport; Self-adjoint equations; Finite-elements

1. Introduction

There are three basic second-order self-adjoint forms of the neutron transport equation: the even-parity (EP) equation, the odd-parity (OP) equation, and the self-adjoint angular flux (SAAF) equation [1,2]. The EP and OP equations have been numerically solved within the neutron transport community for decades

* Corresponding author. Tel.: +1 979 845 4107; fax: +1 979 845 6443.
E-mail address: morel@tamu.edu (J.E. Morel).

0021-9991/$ - see front matter
doi:10.1016/j.jcp.2005.09.017

[3–8]. These equations have been traditionally used to solve only the steady-state neutron transport equation. However, they recently have also been used to solve the non-linear radiative transfer equations [9] and the time-dependent neutron transport equation [10]. Most of the early methods for solving the EP and OP equations used either finite-element or spherical-harmonic approximations for the angular variables. The use of S_n angular discretization was first seen in the 1990s [11,12]. The usual strategy for performing time-dependent calculations is to first discretize the continuum first-order transport equation in time, and then algebraically manipulate the resulting semi-discrete equation to obtain semi-discrete time-dependent EP and OP equations. Ackroyd and de Oliveira [13] have recently derived a maximum principle for the time-dependent, first-order neutron transport equation. This maximum principle can also be used to derive a continuum time-dependent SAAF equation. However, the authors did not use the principle for this purpose, and made no reference to the SAAF equation. The EP, OP and SAAF equations have recently been applied to coupled electron–photon transport [14–16]. This application significantly differs from neutronics and radiative transfer applications because the small energy transfers associated with electron scattering generally requires special treatment. In particular, these transfers can be treated either with a special type of "condensed" cross-section approximation [14,16], or a continuous-slowing-down term [15]. The former is compatible with standard discretization and solution techniques for the EP, OP, and SAAF equations, while the latter requires some generalization of these techniques.

The SAAF equation has only recently been recognized as a valuable alternative to the traditional EP and OP equations [2]. Analogous forms of these equations can be developed for the thermal radiative transfer equations. We refer to these as the even-parity (EP), odd-parity (OP), and self-adjoint angular intensity (SAAI) equations. Since all of these equations are non-linear, they cannot be rigorously self-adjoint. However, they become self-adjoint for the mono-energetic case when linearized. The numerical advantage of these equations is that many of the standard spatial discretization and numerical solution techniques normally applied to the diffusion equation can also be applied to these equations. For instance, when the standard multigroup energy discretization [1] is applied, the linearized equations for each group will be self-adjoint when coupling between groups is ignored. The coupling between groups is lagged in the iterative process used to solve these equations, so an iteration consists of solving an independent second-order self-adjoint equation for each group. Because of the self-adjoint property, one can expect standard finite-element spatial discretization techniques to produce symmetric positive-definite coefficient matrices for each group equation. This in turn makes it possible to use highly developed preconditioned conjugate-gradient methods to solve the iterative equations. Indeed, this is one of the primary numerical advantages of solving self-adjoint forms of the radiative transfer equations as opposed to the standard first-order form. The convergence rate of these group iterations can also be increased significantly using popular diffusion-synthetic acceleration techniques due to these desirable matrix properties.

The purpose of this paper is to describe a general-order, general-geometry, finite-element technique for spatially discretizing the EP, OP, and SAAI thermal radiation transport equations on unstructured meshes. We are unaware of any such method being previously defined for these equations, although our method is certainly analogous in many ways to existing methods for the EP and OP equations for neutron transport. Nonetheless, there is one aspect of our method that appears to be unique relative to all previous methods for the EP and OP transport equations, and this relates to the treatment of the secondary variable. We also give an alternative general-order spatial finite-element technique that can be applied only to the SAAI equation. This alternative method has far fewer unknowns than our "standard" method, but it appears to give comparable accuracy for the test calculations that we considered. Our finite-element techniques are applied in conjunction with backward-Euler temporal differencing and the discrete-ordinates (S_n) angular discretization. The methods trivially accommodate Crank–Nicholson temporal differencing and the spherical-harmonics angular differencing scheme as well.

The remainder of this paper is organized as follows. First, we describe the thermal radiative transfer equations and apply the backward-Euler temporal differencing scheme to them. Next, we describe our general finite-element spatial discretization technique for each of the EP, OP, and SAAI equations. An overview of some of the practical considerations regarding applying the finite-element method to the radiative transfer equations (e.g. mass matrix lumping and the required spatial quadrature order) is also contained in this section. A description of the alternative spatial discretization scheme unique to the SAAI equation is

subsequently provided. A brief overview of the standard techniques used to discretize the remaining angular and energy variables is next given. A basic linearization technique for dealing with the non-linearities in all of the equations is then described. Computational results that demonstrate the validity of our discretization schemes in both one- and two-dimensional Cartesian geometry are given next. Finally, a summary of results and conclusions is provided. A detailed formulation of the boundary conditions for the self-adjoint forms of the radiative transport equations is provided in Appendix A.

2. The standard first-order radiative transfer equations

Using the standard first-order form of the transport equation, the radiative transfer equations can be expressed as follows:

$$\frac{1}{c}\frac{\partial \psi}{\partial t} + \vec{\Omega}\cdot\vec{\nabla}\psi + \sigma_t\psi = \frac{1}{4\pi}\sigma_s\phi + \sigma_a B, \tag{1}$$

and

$$C_v\frac{\partial T}{\partial t} = \int_0^\infty \sigma_a(\phi - 4\pi B)\,\mathrm{d}E, \tag{2}$$

where t denotes time, c denotes the speed of light (length/time), $\vec{\Omega}$ denotes the angular or directional variable (a point on the unit sphere), the gradient is taken with respect to the spatial variables $(x,y,z)\equiv\vec{r}$, E denotes the radiation energy (energy), $\psi(t,\vec{r},\vec{\Omega},E)$ denotes the radiation intensity (energy/area–time–energy–steradian), $T(t,\vec{r})$ denotes the material temperature (keV), $\sigma_t(\vec{r},E,T)$ denotes the macroscopic total cross-section (length^{-1}), the macroscopic scattering cross-section is denoted by $\sigma_s(\vec{r},E,T)$ (length^{-1}), the macroscopic absorption cross-section is denoted by $\sigma_a(\vec{r},E,T)$ (length^{-1}), the specific heat capacity (energy/volume–temperature) is denoted by $C_v(\vec{r},E,T)$, ϕ denotes the angle-integrated intensity,

$$\phi = \int_{4\pi}\psi\,\mathrm{d}\Omega, \tag{3}$$

and $B(E,T)$ (energy/area–time–energy–steradians) denotes the Planck function,

$$B = \frac{2E^3}{h^3c^2}[\exp(E/kT)-1]^{-1}, \tag{4}$$

where h is Planck's constant and k is Boltzmann's constant. We difference Eqs. (1) and (2) in time only using the backward-Euler technique

$$\frac{1}{c\Delta t}(\psi-\psi^n) + \vec{\Omega}\cdot\vec{\nabla}\psi + \sigma_t\psi = \frac{1}{4\pi}\sigma_s\phi + \sigma_a B, \tag{5}$$

and

$$\frac{C_v}{\Delta t}(T-T^n) = \int_0^\infty \sigma_a(\phi - 4\pi B)\,\mathrm{d}E, \tag{6}$$

where n is the time index, Δt is the time step, and every quantity not carrying an index of n is implicitly assumed to carry an index of $n+1$. Thus ψ^n and T^n represent the values of the intensity and temperature, respectively, at the beginning of the time step and all of the other time-dependent quantities are evaluated at the end of the time step.

3. Self-adjoint forms of the radiative transfer equations

In this section, we derive the various self-adjoint forms of the radiative transfer equations from the standard first-order form. The even-parity and odd-parity intensities are, respectively, defined in terms of the intensity as follows:

$$\psi^+ = \frac{1}{2}[\psi(\vec{\Omega}) + \psi(-\vec{\Omega})], \tag{7}$$

$$\psi^- = \frac{1}{2}[\psi(\vec{\Omega}) - \psi(-\vec{\Omega})]. \tag{8}$$

The inverse relationship is

$$\psi = \psi^+ + \psi^-. \tag{9}$$

Note that the angle-integrated intensity is also equal to the angle-integrated even-parity intensity

$$\phi = \int_{4\pi} \psi^+ \, \mathrm{d}\Omega. \tag{10}$$

Substituting $-\vec{\Omega}$ for $\vec{\Omega}$ in Eq. (5), adding the resulting equation to Eq. (5), and dividing by two, we obtain a first-order equation for the even-parity intensity

$$\frac{1}{c\Delta t}(\psi^+ - \psi^{+,n}) + \vec{\Omega} \cdot \vec{\nabla}\psi^- + \sigma_t \psi^+ = \frac{1}{4\pi}\sigma_s \phi + \sigma_a B. \tag{11}$$

Substituting $-\vec{\Omega}$ for $\vec{\Omega}$ in Eq. (5), subtracting the resulting equation from Eq. (5), and dividing by two, we obtain a first-order equation for the odd-parity intensity

$$\frac{1}{c\Delta t}(\psi^- - \psi^{-,n}) + \vec{\Omega} \cdot \vec{\nabla}\psi^+ + \sigma_t \psi^- = 0. \tag{12}$$

Solving Eq. (12) for ψ^-, we get

$$\psi^- = -\frac{1}{\sigma_\tau}\vec{\Omega} \cdot \vec{\nabla}\psi^+ + \frac{Q^-}{\sigma_\tau}, \tag{13}$$

where

$$\tau = \frac{1}{c\Delta t}, \tag{14}$$

$$\sigma_\tau = \sigma_t + \tau, \tag{15}$$

$$Q^- = \tau\psi^{-,n}. \tag{16}$$

Substituting from Eq. (13) into Eq. (11), we obtain a second-order equation for the even-parity intensity:

$$-\vec{\Omega} \cdot \vec{\nabla}\frac{1}{\sigma_\tau}\vec{\Omega} \cdot \vec{\nabla}\psi^+ + \sigma_\tau \psi^+ = Q^+ - \vec{\Omega} \cdot \vec{\nabla}\frac{Q^-}{\sigma_\tau}, \tag{17}$$

where

$$Q^+ = \frac{1}{4\pi}\sigma_s \phi + \sigma_a B + \tau\psi^{+,n}. \tag{18}$$

Eq. (17) is the even-parity equation that we spatially discretize via the finite-element method. When numerically solving this equation, the even-parity intensity is referred to as the primary unknown, and the odd-parity intensity is referred to as the secondary unknown. Since $\psi^+(\vec{\Omega}) = \psi^+(-\vec{\Omega})$, the angular domain for this equation is half that of the standard first-order form of the transport equation; e.g. half the unit sphere in 3-D calculations. Any contiguous half of the unit sphere may be chosen as the domain. Solving Eq. (11) for ψ^+, we get

$$\psi^+ = -\frac{1}{\sigma_\tau}\vec{\Omega} \cdot \vec{\nabla}\psi^- + \frac{Q^+}{\sigma_\tau}. \tag{19}$$

Substituting from Eq. (19) into Eq. (12), we obtain a second-order equation for the odd-parity intensity

$$-\vec{\Omega} \cdot \vec{\nabla}\frac{1}{\sigma_\tau}\vec{\Omega} \cdot \vec{\nabla}\psi^- + \sigma_\tau \psi^- = Q^- - \vec{\Omega} \cdot \vec{\nabla}\frac{Q^+}{\sigma_\tau}. \tag{20}$$

Eq. (20) is the odd-parity equation that we spatially discretize via the finite-element method. When numerically solving this equation, the odd-parity intensity is referred to as the primary unknown, and the even-parity intensity is referred to as the secondary unknown. Since $\psi^-(\vec{\Omega}) = -\psi^-(-\vec{\Omega})$, the angular domain for this equation is half that of the standard first-order form of the transport equation.

Solving Eq. (5) for ψ, we get

$$\psi = -\frac{1}{\sigma_\tau}\vec{\Omega}\cdot\vec{\nabla}\psi + \frac{Q}{\sigma_\tau}, \tag{21}$$

where

$$Q = \frac{1}{4\pi}\sigma_s\phi + \sigma_a B + \tau\psi^n. \tag{22}$$

Substituting from Eq. (21) into the gradient term in Eq. (5), we obtain a second-order equation for the angular intensity

$$-\vec{\Omega}\cdot\vec{\nabla}\frac{1}{\sigma_\tau}\vec{\Omega}\cdot\vec{\nabla}\psi + \sigma_\tau\psi = Q - \vec{\Omega}\cdot\vec{\nabla}\frac{Q}{\sigma_\tau}. \tag{23}$$

Eq. (23) is the SAAI equation that we spatially discretize via the finite-element method. When numerically solving this equation, both the primary and secondary variables represent the angular intensity, but they are represented in different ways. The angular domain for this equation is identical to that of the standard first-order form of the transport equation.

There is an equivalent alternative to the form of the SAAI equation given in Eq. (23). In particular, let us begin its derivation by defining the scattering operator, S, as follows:

$$S\psi = \frac{1}{4\pi}\sigma_s\phi. \tag{24}$$

Then Eq. (21) can be re-expressed as follows:

$$\psi = -(\sigma_\tau - S)^{-1}\vec{\Omega}\cdot\vec{\nabla}\psi + (\sigma_\tau - S)^{-1}\mathcal{Q}, \tag{25}$$

where

$$\mathcal{Q} = \sigma_a B + \tau\psi^n. \tag{26}$$

Substituting from Eq. (25) into the gradient term in Eq. (5), we obtain the alternate form of the SAAI equation

$$-\vec{\Omega}\cdot\vec{\nabla}(\sigma_\tau - S)^{-1}\vec{\Omega}\cdot\vec{\nabla}\psi + \sigma_\tau\psi = S\psi + \mathcal{Q} - \vec{\Omega}\cdot\vec{\nabla}(\sigma_\tau - S)^{-1}\mathcal{Q}. \tag{27}$$

Eq. (23) is usually used with S_n angular discretization, while Eq. (27) is usually used with P_n angular discretization. This is related to differences in the iterative solution techniques used for these methods. Our "standard" finite-element discretization technique has the desirable property that it yields the same numerical solution for both equations given a common angular discretization, i.e., the S_n solution will be the same for both equations and the P_n solution will be the same for both equations. This is not so for our alternative SAAI discretization technique.

4. The finite-element method

In this section we describe our finite-element spatial discretization technique. We first review some of the basic concepts and terms used in the finite-element method [17]. The computational grid is composed of cells or *elements*. For instance, 3-D finite-element grids are usually composed of arbitrary combinations of hexahedra and degenerate hexahedra (wedges, pyramids, and tetrahedra). Each cell has a global index, k, that takes on a value from 1 to K; a volume, V_k; an outer surface, δV_k; and a set of vertices with local indices, $i = 1, P_k$. Each vertex in the grid also has a global index, g, that takes on a value from 1 to G. The outer surface of cell k is the union of the surfaces associated with its faces, i.e.,

$$\delta V_k = \bigcup_{f=1}^{F_k} \delta V_{k,f}, \tag{28}$$

where f is a local face index. Each face that lies on the outer boundary of the grid also has a global index, d, where d takes on a value from 1 to D.

Each cell is associated with a set of local basis functions, $\{\gamma_{k,i}(\vec{r})\}_{i=1}^{P_k}$, which are used to represent the spatial dependence of the "primary" variable within the cell. These local basis functions are identically zero outside of the cell k, and they satisfy

$$\gamma_{k,i}(\vec{r}_{k,j}) = \delta_{i,j}, \tag{29}$$

where $\vec{r}_{k,j}$ denotes the coordinate vector for the vertex with local coordinate j in cell k, and the delta function exhibits the properties:

$$\delta_{i,j} = \begin{cases} 1 & \text{if } i = j, \\ 0, & \text{otherwise.} \end{cases} \tag{30}$$

Thus, these are interpolatory basis functions with interpolation points at the cell vertices. This means that the expansion coefficients for the solutions are just the solution values at the vertices; i.e., an arbitrary function, $h(\vec{r})$, is locally approximated within V_k as follows:

$$\tilde{h}(\vec{r}) = \sum_{i=1}^{P_k} h_{k,i}\gamma_{k,i}(\vec{r}), \quad \vec{r} \in V_k, \tag{31}$$

where

$$h_{k,i} = h(\vec{r}_{k,i}). \tag{32}$$

The global approximation for an arbitrary function, $h(\vec{r})$, can be expressed in terms of the local basis functions as follows:

$$\tilde{h}(\vec{r}) = \sum_{g}^{G} h_g \sum_{n=1}^{N_g} \gamma_{\mathbf{k},\mathbf{i}}(\vec{r}), \tag{33}$$

where

$$h_g = h(\vec{r}_g), \tag{34}$$

N_g denotes the number of cells subtending vertex g; $\mathbf{k} \equiv k(n,g)$ denotes the index of the nth cell subtending vertex g; $\mathbf{i} \equiv i(n,g)$ is the local index of the vertex g in the nth cell subtending vertex g; and $\vec{r}_g$ denotes the coordinate vector for vertex g. It is useful to define global vertex basis functions in addition to the local basis functions. Specifically, the global basis function for vertex g is defined as follows:

$$\beta_g(\vec{r}) = \sum_{n=1}^{N_g} \gamma_{\mathbf{k},\mathbf{i}}(\vec{r}). \tag{35}$$

Using Eq. (35), we can re-express Eq. (33) in a more compact form

$$\tilde{h}(\vec{r}) = \sum_{g}^{G} h_g \beta_g(\vec{r}). \tag{36}$$

4.1. Spatial discretization of the even-parity equation

Our discretization of the even-parity equation begins with Eqs. (6), (11), and (13). The even-parity intensity is the primary unknown. Thus, the discrete even-parity intensities are located on the vertices and expanded in terms of the basis functions, i.e.,

$$\tilde{\psi}^{+}(\vec{r}) = \sum_{g}^{G} \psi_g^{+} \beta_g(\vec{r}). \tag{37}$$

The discrete material temperatures also exist at the vertices and are similarly expanded in the basis functions

$$\widetilde{T}(\vec{r}) = \sum_{g}^{G} T_g \beta_g(\vec{r}). \tag{38}$$

In principle, defining the spatial dependence of the temperature also defines the spatial dependence of the Planckian, $B(T)$. However, this approach is problematic because the Planckian is a non-linear function of temperature. Instead, we define discrete values of the Planckian at the vertices; i.e.,

$$B_g = B(T_g), \quad g = 1, G \tag{39}$$

and expand the Planckian in the basis functions

$$\widetilde{B}(\vec{r}) = \sum_{g}^{G} B_g \beta_g(\vec{r}). \tag{40}$$

To obtain the equation for ψ_g^{+}, we first substitute from Eqs. (14), (15), and (18) into Eq. (11) to obtain

$$\vec{\Omega} \cdot \vec{\nabla} \psi^{-} + \sigma_\tau \psi^{+} = Q^{+}. \tag{41}$$

Next we multiply Eq. (41) by β_g, and analytically integrate over the entire grid

$$\int_V \beta_g [\vec{\Omega} \cdot \vec{\nabla} \psi^{-} + \sigma_\tau \psi^{+} - Q^{+}] \, \mathrm{d}V = 0, \tag{42}$$

where V denotes the entire grid volume. Next we apply Green's Theorem and integrate the gradient term in Eq. (42) by parts to obtain

$$\oint_{\delta V} \beta_g \psi^{-} \vec{\Omega} \cdot \vec{n} \, \mathrm{d}A - \int_V [\psi^{-} \vec{\Omega} \cdot \vec{\nabla} \beta_g] \, \mathrm{d}V + \int_V \beta_g [\sigma_\tau \psi^{+} - Q^{+}] \, \mathrm{d}V = 0, \tag{43}$$

where δV denotes the outer boundary surface of the entire grid and $\vec{n}$ is the outward-directed surface normal. Although ψ^{-} appears in the surface integral in Eq. (43), boundary conditions enable us to express ψ^{-} in terms of ψ^{+} on the surface of the grid. For instance, let us assume a vacuum boundary condition for the purpose of demonstration. More general conditions are discussed in Appendix A, where it shown that for a vacuum boundary condition,

$$\psi^{-} \vec{\Omega} \cdot \vec{n} = \psi^{+} |\vec{\Omega} \cdot \vec{n}| \text{ on } \delta V \quad \text{for all } \vec{\Omega}. \tag{44}$$

Substituting from Eq. (44) into Eq. (43), we get

$$\oint_{\delta V} \beta_g \psi^{+} |\vec{\Omega} \cdot \vec{n}| \, \mathrm{d}A - \int_V [\psi^{-} \vec{\Omega} \cdot \vec{\nabla} \beta_g] \, \mathrm{d}V + \int_V \beta_g [\sigma_\tau \psi^{+} - Q^{+}] \, \mathrm{d}V = 0. \tag{45}$$

Next, we assume the vertex basis function approximations for the even-parity intensity and the Planckian given in Eqs. (37) and (40), respectively, and insert them into Eq. (45)

$$\oint_{\delta V} \beta_g \tilde{\psi}^{+} |\vec{\Omega} \cdot \vec{n}| \, \mathrm{d}A - \int_V [\psi^{-} \vec{\Omega} \cdot \vec{\nabla} \beta_g] \, \mathrm{d}V + \int_V \beta_g [\sigma_\tau \tilde{\psi}^{+} - \widetilde{Q}^{+}] \, \mathrm{d}V = 0, \tag{46}$$

where $\widetilde{Q}^{+}$ denotes the approximation to this quantity resulting from the substitutions. We next substitute the basis function approximation for ψ^{+} into Eq. (13)

$$\psi^{-} = -\frac{1}{\sigma_\tau} \vec{\Omega} \cdot \vec{\nabla} \tilde{\psi}^{+} + \frac{Q^{-}}{\sigma_\tau}. \tag{47}$$

If Q^{-} were zero, we could simply substitute from Eq. (47) into Eq. (46). However, Q^{-} depends upon values of ψ^{-} from the previous time step. Thus we must assign a specific functional dependence to ψ^{-}. Most existing

finite-element methods for the EP and OP neutronics equations were developed only for steady-state calculations. Furthermore, the techniques for representing the secondary variable are straightforward for mono-energetic problems, but generally quite complicated for energy-dependent problems [7]. In steady-state calculations, Q^- is identically zero. This means that the steady-state odd-parity intensities are elements of the space spanned by $\vec{\Omega}\cdot\vec{\nabla}$ operating on the vertex basis functions. Indeed, the existing neutronics methods compute ψ^- directly from $\vec{\Omega}\cdot\vec{\nabla}\psi^+$. This suggests that this "directional-derivative" space should also be used to represent the odd-parity intensities in time-dependent calculations. If the local basis functions for ψ^+ are linear over each cell, then the directional- derivative space is constant over each cell and the functional representation for ψ^- is simple. However, in the general case we have found it cumbersome to use this directional-derivative space to represent the odd-parity intensities, particularly since the space itself depends upon $\vec{\Omega}$ in the general case. For instance, let us consider the tri-linear space of polynomials used to represent the even-parity intensity on hexahedra. Let f be any element of this space. Then f can be represented as follows:

$$f(x,y,z) = c_1 + c_2x + c_3y + c_4z + c_5xy + c_6yz + c_7xz + c_8xyz, \tag{48}$$

where c_1 through c_8 are the coefficients associated with the eight linearly independent basis functions that we have used to define this space. Applying the operator $\vec{\Omega}\cdot\vec{\nabla}$ to f, we get

$$\vec{\Omega}\cdot\vec{\nabla}f = c_2\Omega_x + c_3\Omega_y + c_4\Omega_z + c_5(\Omega_x y + \Omega_y x) + c_6(\Omega_y z + \Omega_z y) + c_7(\Omega_x z + \Omega_z x) + c_8(\Omega_x yz + \Omega_y xz + \Omega_z xy), \tag{49}$$

where Ω_x, Ω_y, and Ω_z, are the x, y, and z components of $\vec{\Omega}$, respectively. Note that there are seven linearly-independent basis functions associated with the directional-derivative space, and further that each basis function is dependent upon $\vec{\Omega}$. While one could certainly use this space to represent ψ^-, we have chosen to use an alternative approach that is much simpler, but no less accurate. Specifically, we use spatial quadrature to perform the volumetric integral containing ψ^- in Eq. (46), and collocate Eq. (47) at the quadrature points. In particular, let $\{\vec{d}_{k,j}, w_{k,j}\}_{j=1}^{D_k}$ denote the set of volumetric quadrature points and weights for cell k, then Eq. (47) is discretized as follows:

$$\psi^-_{k,j} = -\frac{1}{\sigma_\tau}\vec{\Omega}\cdot(\vec{\nabla}\tilde{\psi}^+)_{k,j} + \frac{Q^-_{k,j}}{\sigma_\tau}, \tag{50}$$

where $\psi^-_{k,j}$, $(\vec{\nabla}\tilde{\psi}^+)_{k,j}$, and $Q^-_{k,j}$ denote values for ψ^-, $\vec{\nabla}\tilde{\psi}^+$, and Q^- at quadrature point j in cell k. Thus, we see that the odd-parity intensity and its related quantities (Q^-) are purely discrete and exist at the volumetric quadrature points. Using quadrature to perform the volumetric integral containing ψ^- in Eq. (46) and substituting from Eq. (50) into that equation, we get

$$\oint_{\delta V}\beta_g\tilde{\psi}^+|\vec{\Omega}\cdot\vec{n}|\,\mathrm{d}A - \sum_{n=1}^{N_g}\sum_{j=1}^{D_{\mathbf{k}}}\left\{\left[-\frac{1}{\sigma_\tau}\vec{\Omega}\cdot(\vec{\nabla}\tilde{\psi}^+)_{\mathbf{k},j} + \frac{Q^-_{\mathbf{k},j}}{\sigma_\tau}\right]\vec{\Omega}\cdot(\vec{\nabla}\gamma_{\mathbf{k},\mathbf{i}})_{\mathbf{k},j}\right\}w_{\mathbf{k},j} + \int_V\beta_g[\sigma_\tau\tilde{\psi}^+ - \tilde{Q}^+]\,\mathrm{d}V = 0. \tag{51}$$

We next derive the equation for the discrete temperature unknown at vertex g. First, we substitute the basis functions representations for ψ^+, T, and B, given in Eqs. (37), (38), and (40), respectively, into Eq. (6),

$$\frac{C_v}{\Delta t}(\widetilde{T} - \widetilde{T}^n) = \int_0^\infty \sigma_a(\tilde{\phi} - 4\pi\widetilde{B})\,\mathrm{d}E. \tag{52}$$

Next, we multiply Eq. (52) by the basis function for vertex g and then integrate over the spatial domain to get

$$\int_V\beta_g\left[\frac{C_v}{\Delta t}(\widetilde{T} - \widetilde{T}^n) - \int_0^\infty\sigma_a(\tilde{\phi} - 4\pi\widetilde{B})\,\mathrm{d}E\right] = 0. \tag{53}$$

Because there are no spatial derivatives in Eq. (53), it follows that this equation must hold pointwise at each vertex

$$\frac{C_v}{\Delta t}(T_g - T_g^n) = \int_0^\infty\sigma_a(\phi_g - 4\pi B(T_g))\,\mathrm{d}E. \tag{54}$$

This concludes the derivation of the even-parity finite-element equations. To summarize, there are three fundamental unknowns, the odd-parity intensities that exist at the volumetric quadrature points, the even-parity intensities that exist at the vertices, and the material temperatures that exist at the vertices. The equation for $\psi^-_{k,j}$, the odd-parity angular intensity at quadrature point j in cell k, is given in Eq. (50). The equation for ψ^+_g, the even-parity angular intensity at vertex g, is given in Eq. (51). The equation for T_g, the material temperature at vertex g, is given in Eq. (54).

4.2. Spatial discretization of the odd-parity equation

The basic approach used to discretize the even-parity equations is largely used to discretize the odd-parity equations as well, but the even-parity and odd-parity equations change roles as primary and secondary variables, and hence, exchange location. More specifically, the odd-parity intensities are located at the vertices and the even-parity intensities are located at the quadrature points. For instance, collocating Eq. (19) at quadrature point j of element k, we obtain the even-parity analog of Eq. (50)

$$\psi^+_{k,j} = -\frac{1}{\sigma_\tau}\vec{\Omega}\cdot(\vec{\nabla}\tilde{\psi}^-)_{k,j} + \frac{Q^+_{k,j}}{\sigma_\tau}. \tag{55}$$

The temperatures must be co-located with the even-parity intensities, so they are also located at the quadrature points. Collocating Eq. (6) at quadrature point j in cell k yields

$$\frac{C_v}{\Delta t}(T_{k,j} - T^n_{k,j}) = \int_0^\infty \sigma_a(\phi_{k,j} - 4\pi B(T_{k,j}))\,\mathrm{d}E. \tag{56}$$

Using the vertex basis functions to represent the odd-parity intensities in Eq. (20), and proceeding in analogy with the discretization steps for Eq. (17), we obtain the odd-parity analog to Eq. (51)

$$\oint_{\delta V}\beta_g\tilde{\psi}^-|\vec{\Omega}\cdot\vec{n}|\,\mathrm{d}A - \sum_{n=1}^{N_g}\sum_{j=1}^{D_\mathbf{k}}\left\{\left[-\frac{1}{\sigma_\tau}\vec{\Omega}\cdot(\vec{\nabla}\tilde{\psi}^-)_{\mathbf{k},j} + \frac{Q^+_{\mathbf{k},j}}{\sigma_\tau}\right]\vec{\Omega}\cdot(\vec{\nabla}\gamma_{\mathbf{k},\mathbf{i}})_{\mathbf{k},j}\right\}w_{\mathbf{k},j} + \int_V \beta_g[\sigma_\tau\tilde{\psi}^- - \tilde{Q}^-]\,\mathrm{d}V = 0. \tag{57}$$

This completes the derivation of the odd-parity finite-element equations, which consist of Eqs. (55)–(57).

4.3. Standard spatial discretization of the SAAI equation

We first derive the standard discretization scheme for the SAAI equation. It can be shown that the sum of the analytic even-parity and odd-parity equations is the self-adjoint angular intensity equation [2]. This follows largely from Eq. (9). For this reason, the finite-element approach used to discretize the even-parity and odd-parity equations can be directly applied to the SAAI equation simply by summing the discrete even-parity and odd-parity equations. There are useful alternatives to the boundary treatments obtained in this way that were applied to the SAAF equation in [2]. The merits of these alternative conditions are discussed in Appendix A. It follows from the summation principle that the SAAI discretization has angular intensity and temperature unknowns at *both* the vertices and the quadrature points. The angular intensities at the vertices are considered the primary unknowns and the angular intensities at the quadrature points are considered the secondary unknowns.

Summing Eqs. (50) and (55), we obtain the equation for the angular intensity at quadrature point j in cell k

$$\psi_{k,j} = -\frac{1}{\sigma_\tau}\vec{\Omega}\cdot(\vec{\nabla}\tilde{\psi})_{k,j} + \frac{Q_{k,j}}{\sigma_\tau}. \tag{58}$$

The equation for the temperature at quadrature point j in cell k is given by Eq. (56) (the *only* temperature equation for the odd-parity equations). The equation for the temperature at vertex g is given by Eq. (54) (the *only* temperature equation for the even-parity equations). The equation for the angular intensity at vertex g is obtained by adding Eqs. (51) and (57)

$$\oint_{\delta V} \beta_g \tilde{\psi} |\vec{\Omega} \cdot \vec{n}| \, \mathrm{d}A - \sum_{n=1}^{N_g} \sum_{j=1}^{D_{\mathbf{k}}} \left\{ \left[-\frac{1}{\sigma_\tau} \vec{\Omega} \cdot (\vec{\nabla} \tilde{\psi})_{\mathbf{k},j} + \frac{Q_{\mathbf{k},j}}{\sigma_\tau} \right] \vec{\Omega} \cdot (\vec{\nabla} \gamma_{\mathbf{k},\mathbf{i}})_{\mathbf{k},j} \right\} w_{\mathbf{k},j} + \int_V \beta_g [\sigma_\tau \tilde{\psi} - \widetilde{Q}] \, \mathrm{d}V = 0. \quad (59)$$

This completes the derivation of the standard finite-element discretization for the SAAI equation, which consists of Eqs. (54), (56), (58), and (59).

It is not difficult to show that solving the SAAI equation with the standard discretization is completely equivalent to solving both the even-parity and odd-parity equations, provided that the SAAI boundary conditions are consistent with both the even-parity and odd-parity boundary conditions. These consistent SAAI conditions are referred to as the "parity-equivalent" conditions in Appendix A. The solutions are equivalent in the sense that SAAI solution is simply the sum of the even-parity and odd-parity solutions.

4.4. Averaging of even-parity and odd-parity solutions

It is well-known within the neutron transport community that averaging finite-element even-parity solutions with odd-parity solutions can result in very accurate solutions under a variety of conditions [18]. For instance, it has been shown [19,20] that amazingly accurate scalar flux solutions can be obtained in highly diffusive 1-D steady-state problems with unresolved spatial boundary layers by averaging vertex-centered scalar fluxes from an even-parity calculation with cell-centered scalar fluxes from an odd-parity calculation. It has also been shown that the same solutions can be obtained by averaging vertex-centered and cell-centered scalar fluxes obtained from a parity-equivalent SAAF calculation [21]. Such properties might be quite valuable in radiative transfer calculations since adequately resolving boundary layers can sometimes be prohibitively expensive in such calculations. However, it is not obvious that properties which hold for steady-state self-adjoint neutron transport calculations necessarily hold for time-dependent non-linear self-adjoint radiative transfer calculations. We later present computational results which indicate that our self-adjoint radiative transfer discretizations retain these highly desirable properties. These properties are lost with the standard SAAI discretization when the boundary treatment defined by Eqs. (A.17) and (A.18) (which are given in Appendix A) is used. In this case, the SAAI solution is no longer parity-equivalent. However, there is evidence that this more physical boundary condition results in vertex-centered scalar fluxes that are more accurate than those obtained with the parity-equivalent boundary conditions [2]. Finally, we note that the alternative SAAI discretization derived in the following section cannot have these averaging properties because it has only vertex-centered unknowns. Thus, it cannot be made equivalent to the even-parity and odd-parity discretizations.

4.5. Spatial quadrature order

To our knowledge, defining the secondary variables at the volumetric quadrature points via collocation is a unique aspect of our approach. Its advantages are that it is both simple and accurate. For instance, let us consider the even-parity equations without loss of generality. Ideally, one would like to solve Eq. (47) exactly given $\vec{\Omega} \cdot \vec{\nabla} \tilde{\psi}^+$. Under our approach, Eq. (47) is exactly solved at the quadrature points. Thus any additional approximation associated with our approach must arise from the use of quadrature to evaluate the integrals in Eq. (46). However, there is actually no additional approximation because the quadratures we use are exact whenever the integrals in Eq. (46) can be evaluated analytically, and quadrature is always used in standard finite-element methods if the integrals cannot be evaluated analytically [17]. The only disadvantage of our approach is that the secondary variables generally require much more computer storage than the primary variables. For instance, on an orthogonal hexahedral mesh with tri-linear basis functions, there are eight times more secondary variables than primary variables using an eight-point Gauss quadrature.

It is clearly desirable to minimize the order of the volumetric quadrature while maintaining the maximum order accuracy of the solution. The issue of optimal quadrature order is discussed in [17]. For instance, using a linear trial-space on tetrahedra, one can obtain second-order accuracy using a one-point volumetric quadrature and one-point surface quadrature. However, all of the integrals can be exactly evaluated using a one-point volumetric quadrature for the integrals containing basis function gradients, a four-point quadrature for the removal and source integrals, and a three-point quadrature for the surface integrals. Since the intensity

unknowns at the volumetric quadrature points are associated only with the quadrature set used for the gradient integrals, this approach results in exact integration with only one intensity unknown per tetrahedron. In contrast, using a tri-linear trial space on general hexahedra, one cannot obtain exact integration for all terms regardless of the quadrature order used. However, one can obtain second-order accuracy of the solution using an eight-point volumetric Gauss quadrature and a four-point Gauss surface quadrature. The removal, source, and surface integrals will be exact with these quadratures, but the gradient integrals will not be. These are the types of issues that should be considered when choosing a quadrature order.

4.6. Finite-element lumping

Our experience with radiative transfer problems in the stellar regime indicates that finite-element lumping [17] of the removal and source terms is often desirable for increased robustness. The traditional concept of lumping only applies to the removal and source terms (analogous to so-called mass matrix lumping [17] in structural finite-elements). It is also desirable to lump the gradient term, but this remains a research topic for unstructured meshes. Hence we only describe removal/source lumping here. The removal and source terms in Eqs. (51) and (57) are lumped by making the following respective replacements:

$$\int_V \beta_g[\sigma_\tau \tilde{\psi}^+ - \widetilde{Q}^+]\,\mathrm{d}V \to \psi_g^+ \int_V \sigma_\tau \beta_g\,\mathrm{d}V - Q_g^+ \int_V \beta_g\,\mathrm{d}V, \tag{60}$$

$$\int_V \beta_g[\sigma_\tau \tilde{\psi}^- - \widetilde{Q}^-]\,\mathrm{d}V \to \psi_g^- \int_V \sigma_\tau \beta_g\,\mathrm{d}V - Q_g^- \int_V \beta_g\,\mathrm{d}V. \tag{61}$$

The removal and source terms in our standard and alternative differenced SAAI equations, Eqs. (59) and (71), respectively, are lumped by making the following replacement:

$$\int_V \beta_g[\sigma_\tau \tilde{\psi} - \widetilde{Q}]\,\mathrm{d}V \to \psi_g \int_V \sigma_\tau \beta_g\,\mathrm{d}V - Q_g \int_V \beta_g\,\mathrm{d}V. \tag{62}$$

4.7. Unstructured mesh basis functions

The basis functions for non-orthogonal elements are constructed in a rather special manner. In particular, the basis functions are defined with respect a "local" coordinate system rather than the global or physical coordinate system used to define the grid. A local coordinate system is used because the finite-element integrations are generally much easier to express in the local system. Thus all integrations are carried out in the local system. Furthermore, the integrals for non-orthogonal elements generally cannot be analytically performed, so a quadrature is usually used to perform them. For simplicity, we have chosen to ignore these complications in our finite-element equations. However, the fully detailed expressions are easily obtained from our expressions. For instance, let $\vec{s} = (s_1, s_2, s_3)$ denote the local coordinates, and let $\vec{r} = (r_1, r_2, r_3)$ denote the global coordinates. The gradient of vertex basis function g at global position $\vec{r}$ is expressed as follows:

$$\vec{\nabla}_r \beta_g(\vec{r}) = \mathscr{J}^{-1} \vec{\nabla}_s \beta_g(\vec{s}), \tag{63}$$

where $\mathscr{J}$ is the Jacobian matrix associated with the mapping from the local to global coordinate system. The global volume element is given in terms of the local volume element as follows:

$$\mathrm{d}r_1\,\mathrm{d}r_2\,\mathrm{d}r_3 = |\mathscr{J}|\,\mathrm{d}s_1\,\mathrm{d}s_2\,\mathrm{d}s_3, \tag{64}$$

where $|\mathscr{J}|$ denotes the determinant of the Jacobian matrix. This implies that a volumetric quadrature weight in the global system is expressed in terms of the local quadrature weight as follows:

$$w_r = |\mathscr{J}| w_s, \tag{65}$$

where the Jacobian is evaluated at the quadrature point associated with w_s. Similar relationships exist for the surface integrals. Complete details are given in [17].

5. Alternative spatial discretization of the SAAI equation

We next derive the alternative finite-element scheme for the SAAI equation. This derivation is begun by assuming that all of the unknowns exist at the vertices, and representing these unknowns in terms of the vertex basis functions. Thus, the basis function representations for the material temperature and the Planckian are, respectively, given by Eqs. (38) and (40), while the representation for the angular intensity is given by

$$\tilde{\psi}(\vec{r}) = \sum_{g}^{G} \psi_g \beta_g(\vec{r}). \tag{66}$$

Substituting the angular intensity and Planckian representations into the SAAI equation, Eq. (23), we obtain

$$\vec{\Omega} \cdot \vec{\nabla} \left[-\frac{1}{\sigma_\tau} \vec{\Omega} \cdot \vec{\nabla} \tilde{\psi} + \frac{\widetilde{Q}}{\sigma_\tau} \right] + \sigma_\tau \tilde{\psi} - \widetilde{Q} = 0, \tag{67}$$

where $\widetilde{Q}$ denotes the approximation to this quantity resulting from the substitutions. Next, we multiply Eq. (67) by β_g and integrate over the entire spatial domain

$$\int_V \beta_g \vec{\Omega} \cdot \vec{\nabla} \left[-\frac{1}{\sigma_\tau} \vec{\Omega} \cdot \vec{\nabla} \tilde{\psi} + \frac{\widetilde{Q}}{\sigma_\tau} \right] \mathrm{d}V + \int_V \beta_g [\sigma_\tau \tilde{\psi} - \widetilde{Q}] \, \mathrm{d}V = 0. \tag{68}$$

Integrating the gradient term in Eq. (68) by parts, we get

$$\oint_{\delta V} \beta_g \left[-\frac{1}{\sigma_\tau} \vec{\Omega} \cdot \vec{\nabla} \tilde{\psi} + \frac{\widetilde{Q}}{\sigma_\tau} \right] \vec{\Omega} \cdot \vec{n} \, \mathrm{d}A - \int_V \left[-\frac{1}{\sigma_\tau} \vec{\Omega} \cdot \vec{\nabla} \tilde{\psi} + \frac{\widetilde{Q}}{\sigma_\tau} \right] \vec{\Omega} \cdot \vec{\nabla} \beta_g \, \mathrm{d}V + \int_V \beta_g [\sigma_\tau \tilde{\psi} - \widetilde{Q}] \, \mathrm{d}V = 0. \tag{69}$$

Substituting from Eq. (21) into the surface integral in Eq. (69), we get

$$\oint_{\delta V} \beta_g \tilde{\psi} \vec{\Omega} \cdot \vec{n} \, \mathrm{d}A - \int_V \left[-\frac{1}{\sigma_\tau} \vec{\Omega} \cdot \vec{\nabla} \tilde{\psi} + \frac{\widetilde{Q}}{\sigma_\tau} \right] \vec{\Omega} \cdot \vec{\nabla} \beta_g \, \mathrm{d}V + \int_V \beta_g [\sigma_\tau \tilde{\psi} - \widetilde{Q}] \, \mathrm{d}V = 0. \tag{70}$$

The surface integral in Eq. (70) was obtained without any consideration of boundary conditions. For purposes of demonstration, we impose the vacuum condition and use the same treatment used in Eq. (59)

$$\oint_{\delta V} \beta_g \tilde{\psi} |\vec{\Omega} \cdot \vec{n}| \, \mathrm{d}A - \int_V \left[-\frac{1}{\sigma_\tau} \vec{\Omega} \cdot \vec{\nabla} \tilde{\psi} + \frac{\widetilde{Q}}{\sigma_\tau} \right] \vec{\Omega} \cdot \vec{\nabla} \beta_g \, \mathrm{d}V + \int_V \beta_g [\sigma_\tau \tilde{\psi} - \widetilde{Q}] \, \mathrm{d}V = 0. \tag{71}$$

More general boundary conditions and alternative boundary treatments are given in Appendix A. This completes the derivation of the alternative SAAI finite-element equations, which consist of Eqs. (54) and (71).

6. Angular discretization

Since spatial discretization is the focus of this paper, we consider only the S_n [1] angular discretization method. However, we should note that the P_n, or spherical-harmonic, method is an alternative to the S_n method that has been traditionally used in conjunction with self-adjoint forms of the transport equation. These two discretization techniques are complimentary in their strengths and weaknesses. We used the S_n discretization in this study primarily because it is easier to implement.

The S_n method is most easily characterized as an angular collocation method. The collocation points also correspond to a set of quadrature directions. This quadrature set is used to calculate the angle-integrated intensity from the discrete angular intensities. For instance, let $\{\vec{\Omega}_m, W_m\}_{m=1}^{M}$ denote an angular quadrature set where $\vec{\Omega}_m$ is the mth direction and W_m is the mth weight. Applying the S_n discretization to the SAAI equation, Eq. (23), we obtain

$$-\vec{\Omega}_m \cdot \vec{\nabla} \frac{1}{\sigma_\tau} \vec{\Omega}_m \cdot \vec{\nabla} \psi_m + \sigma_\tau \psi_m = Q_m - \vec{\Omega}_m \cdot \vec{\nabla} \frac{Q_m}{\sigma_\tau}, \quad m = 1, M, \tag{72}$$

where

$$Q_m = \frac{1}{4\pi}\sigma_s \sum_{m'=1}^{M} \psi_{m'} W_k + \sigma_a B + \tau \psi_{m'}^n. \tag{73}$$

One can also obtain Eq. (73) by first applying the S_n angular discretization to the first-order Eqs. (5) and (21), and then substituting from Eq. (21) into Eq. (5). The standard angularly discretized finite-element SAAI equations are obtained by applying the S_n angular discretization to Eqs. (58) and (59), and using the S_n expression for ϕ in Eqs. (54) and (56), i.e.,

$$\phi = \sum_{m=1}^{M} \psi_m^+ W_m. \tag{74}$$

A standard S_n quadrature set has N directions in 1-D, $N(N+1)/2$ directions in 2-D, and $N(N+1)$ directions in 3-D. The even-parity and odd-parity fluxes need be defined at only half of the quadrature directions because of the symmetry of ψ^+ and the anti-symmetry of ψ^- with respect to a change in the sign of $\vec{\Omega}$.

7. Energy discretization

We use the standard multigroup method [1] to discretize the self-adjoint equations in photon energy. This approximation is based upon a contiguous set of energy intervals or "groups" that span the energy domain. Since all of the time-discretized self-adjoint equations are derived from the time-discretized first-order form of the transport equation, it suffices to give the multigroup discretization for this equation:

$$\frac{1}{c\Delta t}(\psi_q - \psi_q^n) + \vec{\Omega}\cdot\vec{\nabla}\psi_q + \sigma_{t,q}\psi_q = \frac{1}{4\pi}\sigma_{s,q}\phi_q + \sigma_{a,q}B_q, \quad q = 1, N_q, \tag{75}$$

where q is the energy group index, ψ_q is the angular intensity integrated over group q, ϕ_q is the angle-integrated intensity integrated over group q, B_q is the Planck function integrated over group q, $\sigma_{t,q}$ is the macroscopic total cross-section averaged over group q, $\sigma_{s,q}$ is the macroscopic scattering cross-section averaged over group q, and N_q is the total number of energy groups.

8. Solution of the equations

We use Newton's method to solve the self-adjoint equations, but the contributions from the material properties are not included in the Jacobian. For instance, let T^* denote the latest Newton iterate for the temperature. Then the linearized equations for the next Newton iteration are obtained by evaluating the material properties at T^* and expanding the Planck function temperature dependence about T^* as follows:

$$B_q^{n+1} = B_q^* + \frac{\partial B_q^*}{\partial T}(T^{n+1} - T^*), \tag{76}$$

where a superscript "$*$" denotes a quantity evaluated at T^*. With the above expansion, the material temperature can be eliminated from the transport equation. In particular, the linearized temporally-differenced first-order multigroup transport equation can be expressed as follows:

$$\vec{\Omega}\cdot\vec{\nabla}\psi_q + \sigma_{\tau,q}^*\psi_q = \frac{1}{4\pi}\sigma_{s,q}^*\phi_q + \frac{1}{4\pi}\nu\chi_q \sum_{q'=1}^{N_q} \sigma_{a,q'}^*\phi_{q'} + \xi_q, \quad q = 1, N_q, \tag{77}$$

where

$$\nu = \frac{4\pi\sum_{q=1}^{N_q}\sigma_{a,q}^*\frac{\partial B_q^*}{\partial T}}{\frac{C_v^*}{\Delta t} + 4\pi\sum_{q=1}^{N_q}\sigma_{a,q}^*\frac{\partial B_q^*}{\partial T}}, \tag{78}$$

$$\chi_q = \frac{\sigma^*_{a,q}\frac{\partial B^*_q}{\partial T}}{\sum_{q'=1}^{N_q}\sigma^*_{a,q'}\frac{\partial B^*_{q'}}{\partial T}}, \tag{79}$$

$$\xi_q = \sigma^*_{a,q}B^*_q + \tau\psi^n_q - \frac{1}{4\pi}v\chi_q\left[4\pi\sum_{q'=1}^{N_q}\sigma^*_{a,q'}B^*_{q'} + C^*_v(T^* - T^n)\right], \tag{80}$$

and the material temperature is given by

$$T^{n+1} = T^* + \frac{\sum_{q=1}^{N_q}\sigma^*_{a,q}\phi_q - 4\pi\sum_{q=1}^{N_q}\sigma^*_{a,q}B^*_q + C^*_v(T^* - T^n)}{\frac{C^*_v}{\Delta t} + 4\pi\sum_{q=1}^{N_q}\sigma^*_{a,q}\frac{\partial B^*_q}{\partial T}}. \tag{81}$$

Eq. (81) is used to calculate the temperatures after the linearized transport equation has been solved.

Our spatial discretizations for the self-adjoint equations can yield negative solutions when stressed. In general, such negativities are small, but they can nonetheless cause the solution algorithm to fail when evaluating the Planck function and the material properties. We attempt to avoid these difficulties by making special definitions for the material properties at negative temperatures. For instance, let T^* be any positive temperature. Each material property is defined at $-T^*$ simply by evaluating that property at the floor (i.e., initial) problem temperature T_{floor}; e.g. $\sigma_t(-T^*) = \sigma_t(T_{\text{floor}})$. The material properties must remain positive to avoid unstable solutions. The Planck function is defined at $-T^*$ by evaluating the Planck function at T^* and then multiplying the resulting value by -1; e.g. $B(-T^*) = -B(T^*)$. The derivative of the Planck function is analogously defined: $\frac{\partial B}{\partial T}(-T^*) = -\frac{\partial B}{\partial T}(T^*)$. Since a negative intensity contributes to a negative time derivative of the temperature, the Planck function at negative temperatures should similarly contribute to a negative time derivative of the intensity. This implies that the Planck function at negative temperatures should be negative. Using these definitions for negative temperatures gives us a system of equations that appears to be very well behaved in the presence of negative intensities and temperatures. It has been our experience that the Newton iterations converge and suffer only slight degradation in convergence rate with negative intensities and any associated negative temperatures. Nonetheless, we must point out that this scheme is new and has only been used on a limited number of problems. Although we have not seen it fail, we cannot guarantee that it is unconditionally effective.

The linearized equations associated with each Newton iteration are solved via the standard source-iteration technique. This iteration is carried out on two nested levels, but for illustrative purposes we initially assume a single level. The one-level source iteration process for the first-order equation can be represented as follows:

$$\vec{\Omega}\cdot\vec{\nabla}\psi^{\ell+1}_q + \sigma^*_{\tau,q}\psi^{\ell+1}_q = \frac{1}{4\pi}\sigma^*_{s,q}\phi^\ell_q + \frac{1}{4\pi}v\chi_q\sum_{q'=1}^{N_q}\sigma^*_{a,q'}\phi^\ell_{q'} + \xi_q, \quad q = 1, N_q, \tag{82}$$

where ℓ is the integration index. We refer to source terms in Eq. (82) containing σ_s and σ_a, as the scattering and implicit emission sources, respectively. The operator on the left side of Eq. (82) consists of an independent first-order equation for each direction and energy group that corresponds to a block lower-triangular matrix after spatial discretization. Each block consists of the equations for a single cell. These equations are relatively easy to solve.

The self-adjoint source iteration equations can be derived directly from Eq. (82). For instance, this results in the following SAAI source iteration equations:

$$-\vec{\Omega}\cdot\vec{\nabla}\frac{1}{\sigma^*_{\tau,q}}\vec{\Omega}\cdot\vec{\nabla}\psi_q + \sigma^*_{\tau,q}\psi_q = \Lambda^\ell_q - \vec{\Omega}\cdot\vec{\nabla}\frac{\Lambda^\ell_q}{\sigma^*_{\tau_q}}, \tag{83}$$

where

$$\Lambda^\ell = \frac{1}{4\pi}\sigma^*_{s,q}\phi^\ell_q + \frac{1}{4\pi}v\chi_q\sum_{q'=1}^{N_q}\sigma^*_{a,q'}\phi^\ell_{q'} + \xi_q. \tag{84}$$

Note that the operator on the left side of Eq. (83) consists of an independent second-order equation for each direction and energy. When spatially discretized, each equation corresponds to a sparse symmetric positive-

definite matrix. Such matrices can generally be efficiently solved using preconditioned conjugate-gradient techniques. Analogous source iteration equations are obtained for the other self-adjoint forms of the transport equation.

The true source iteration process nests the scattering source iterations within the implicit emission source iterations. Thus the scattering source iterations are referred to as the inner iterations and the emission source iterations are referred to as the outer iterations. This is completely analogous to the source iteration process for neutron transport with the photon scattering and emission sources corresponding to the neutron within-group scattering and fission sources, respectively [1]. The scattering source iterations can be accelerated using diffusion-synthetic acceleration (DSA) [12], and the emission iterations can be accelerated using linear multi-frequency-grey acceleration (LMGA) [22]. A detailed discussion of these schemes is beyond the scope of this paper.

9. Computational results

This section details the calculations that were performed to test our finite-element spatial discretization techniques. We consider only the SAAI equation because the standard SAAI discretization is directly related to those for the even-parity and odd-parity equations. One-dimensional Cartesian geometry research codes were generated for both the standard and alternative SAAI equations using linear continuous basis functions. Standard finite-element lumping of the source and removal operators was employed to increase the robustness of the schemes. Such lumping reduces accuracy, but maintains the order of accuracy of the unlumped scheme. A two-dimensional, Cartesian geometry, spatially bi-linear continuous code was generated using the alternative SAAI discretization scheme. The grey (one-group) approximation was applied to the energy variable in all of our calculations. All of the SAAI calculations were performed using the solution technique described in the previous section. An Implicit Monte-Carlo (IMC) code was used to provide solutions for comparison with the SAAI solutions [23,24].

9.1. One-dimensional results

A standard Marshak wave benchmark problem [25] was selected for 1-D testing of our two discretization schemes for the SAAI equation. This test case consists of an isotropic black-body boundary source at a temperature of 1 keV impinging upon a slab with a thickness of 0.05 cm and an initial spatially-uniform temperature of 1 eV. The slab material properties are defined by the temperature-dependent macroscopic absorption cross-section, a null scattering cross-section, and a constant heat capacity. The macroscopic absorption cross-section is given by $\sigma_a = 300/(T^3)$ cm^{-1} with T in keV. The heat capacity has a value of $0.3\,\frac{\text{Jks}}{\text{cm}^3-\text{keV}}$ (1 Jks $= 10^9$ J). A constant time step size of $\Delta t = 1.25 \times 10^{-6}$ shakes (1 shake $= 10^{-8}$ s) was determined sufficient to achieve a fully time-converged solution based upon preliminary calculations. The Marshak benchmark problems were run using S_2 angular quadrature. The "parity-equivalent" source boundary conditions, defined by Eqs. (A.15) and (A.16) in Appendix A, were used in the SAAI calculations for both discretizations. Unless otherwise stated, comparisons between the standard and alternative SAAI discretization are made in terms of the primary (vertex-centered) solutions.

The first set of calculations that we consider was performed to demonstrate the accuracy of the standard and alternative SAAI discretizations relative to that of certain established schemes. Solutions for the Marshak problem were obtained using the standard SAAI discretization (SAAI-S), the alternative SAAI discretization (SAAI-A), a standard linear discontinuous discretization of the first-order form of the radiative transfer equation (LD-1ST) [26], and the standard Implicit Monte-Carlo method [23]. The SAAI calculations and the linear-discontinuous calculations were carried out with 100 uniform spatial cells. The Monte-Carlo calculation was carried out with only 10 spatial cells to reduce statistical error. These solutions are compared in Fig. 1 at a time of 0.1 shakes. It can be seen from Fig. 1 that the SAAI-S, SAAI-A, and LD-1ST solutions show excellent agreement with each other. They also show excellent agreement with the IMC solution except at points near the wavefront. However, since the IMC calculation was performed with only 10 cells, a proper comparison requires that the other solutions be averaged over the Monte-Carlo cell containing the wavefront. When this is done, it is found that the IMC calculation is in good agreement with the other calculations.

As noted in Section 4.4, it has been demonstrated for the case of 1-D steady-state neutron transport calculations that averaging of the vertex-centered and cell-centered scalar flux solutions from the standard parity-equivalent SAAF discretization yields a significantly improved scalar flux solution [21]. The second set of calculations that we consider was performed to investigate whether the parity-equivalent SAAI discretization has an analogous property for the angle-integrated intensity in a 1-D time-dependent non-linear problem. To obtain a coarse-mesh solution for averaging, the Marshak problem was performed with the standard SAAI discretization using only 20 spatial cells. The 20-cell (coarse-mesh) solutions are compared with 100-cell (fine-mesh) solutions at various times in Fig. 2. The vertex-centered angle-integrated intensity distributions, the cell-centered angle-integrated intensity distributions, and an average of those two distributions are plotted. It can be seen from Fig. 2 that the averaged distributions show excellent agreement with the fine-mesh distributions at all times, while the vertex distributions are consistently low, and the cell-centered distributions are consistently high. These results clearly indicate that a much more accurate solution is indeed obtained by averaging the vertex and cell-centered solutions in SAAI calculations with the standard discretization.

The third set of calculations that we consider was performed to confirm the expectation that standard SAAI discretization is more accurate than the alternative SAAI discretization if one compares the vertex-centered solutions from each scheme. A comparison of the standard and alternative SAAI radiation temperature distributions at various times for the Marshak problem are compared in Fig. 3 for the case of 20 spatial cells, and in Fig. 4 for the case of 50 spatial cells. A similar comparison for the case of 100 cells at 0.1 shakes was previously illustrated in Fig. 1. It can be seen from these three figures that the alternative SAAI solutions rapidly converge to those of the standard scheme as the mesh is refined. The former method has half the number of unknowns as the latter in 1-D calculations, however, resulting in a significant reduction in data storage requirements. The reduction in unknowns becomes even more significant in 2-D and 3-D and with higher-order basis sets. For example, the standard discretization scheme for the SAAI equations requires eight times the storage of the alternative discretization for 3-D hexahedral-mesh calculations. A complete exploration of the relative efficiency of the two schemes is beyond the scope of this paper. Nonetheless, it is clear that for the 1-D case, the alternative scheme is comparable in accuracy to the standard scheme when the total number of unknowns is similar for both methods, and one is comparing vertex-centered solutions.

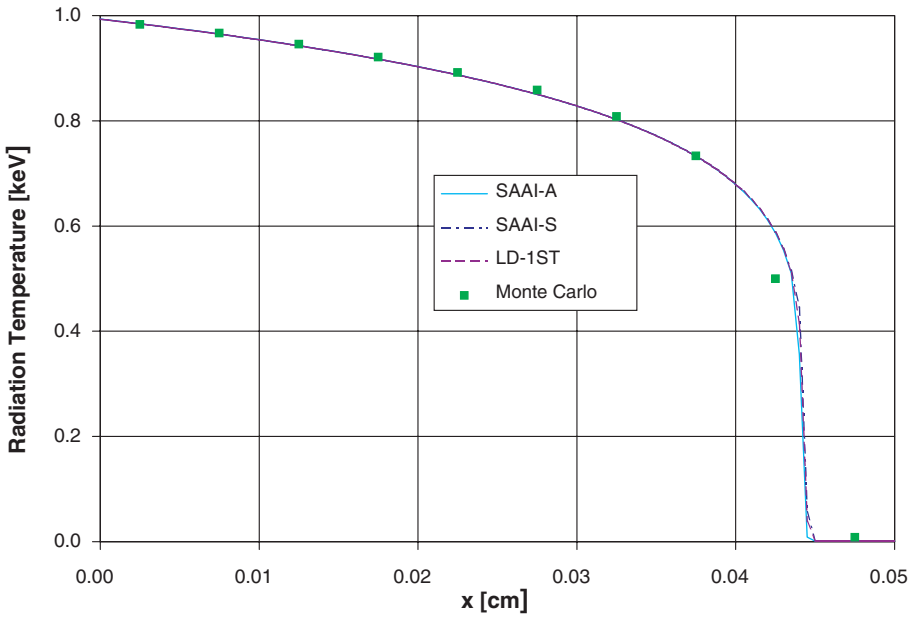

Fig. 1. Comparison of Marshak wave solutions at 0.1 shakes. "SAAI-S" refers to the standard SAAI discretization, "SAAI-A" refers to the alternative SAAI discretization, "LD-1ST" refers to a linear-discontinuous method for the first-order form of the radiative transfer equations, and "Monte-Carlo" refers to the standard Implicit Monte-Carlo method.

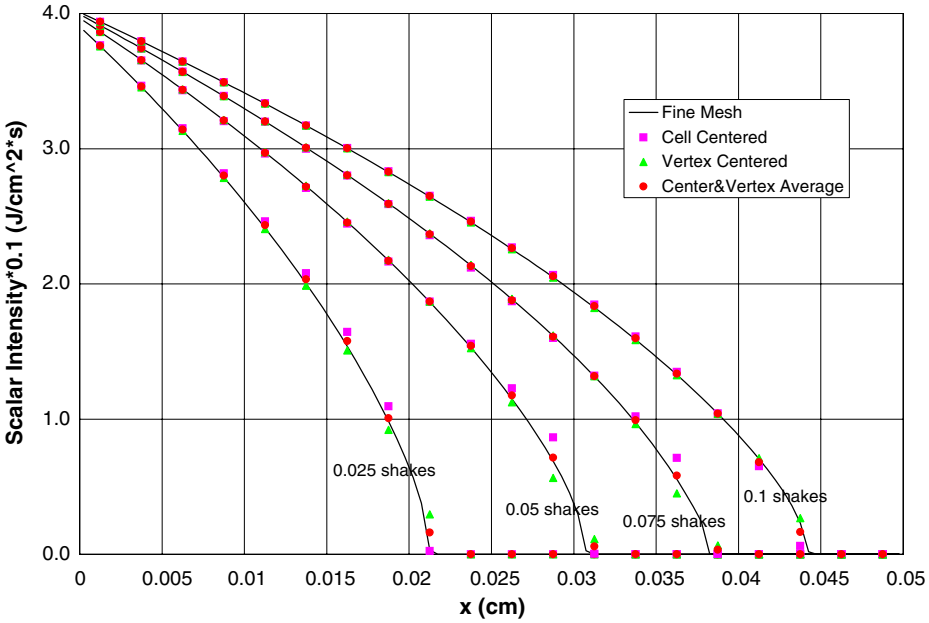

Fig. 2. Marshak solutions with standard SAAI differencing, and cell and vertex averaging.

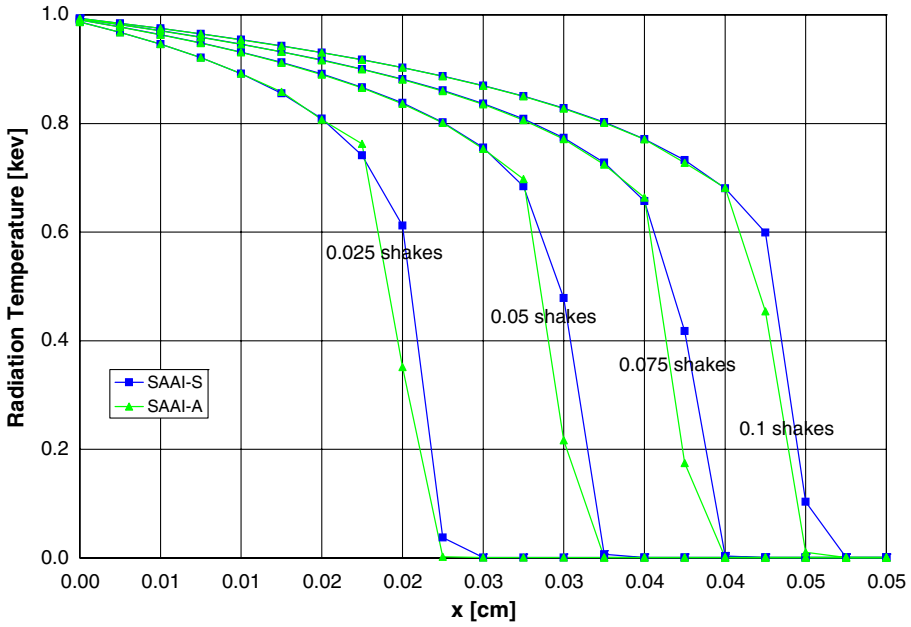

Fig. 3. Comparison of the standard and alternative SAAI discretizations with 20 spatial cells.

The fourth set of calculations was performed to demonstrate that the standard SAAI scheme is somewhat more robust than the alternative SAAI scheme. Toward this end, the Marshak wave problem was modified slightly by inserting an optically-thin region of width 0.025 cm, with an absorption cross-section of $\sigma_a = \frac{0.003}{T^3}$ cm^{-1} in the center of the slab. This creates a central optically-thin region surrounded by two optically-thick regions of equal thickness. Each region was meshed with 50 cells. The problem geometry allows the radiation field to stream through the optically-thin region with very little attenuation and, subsequently,

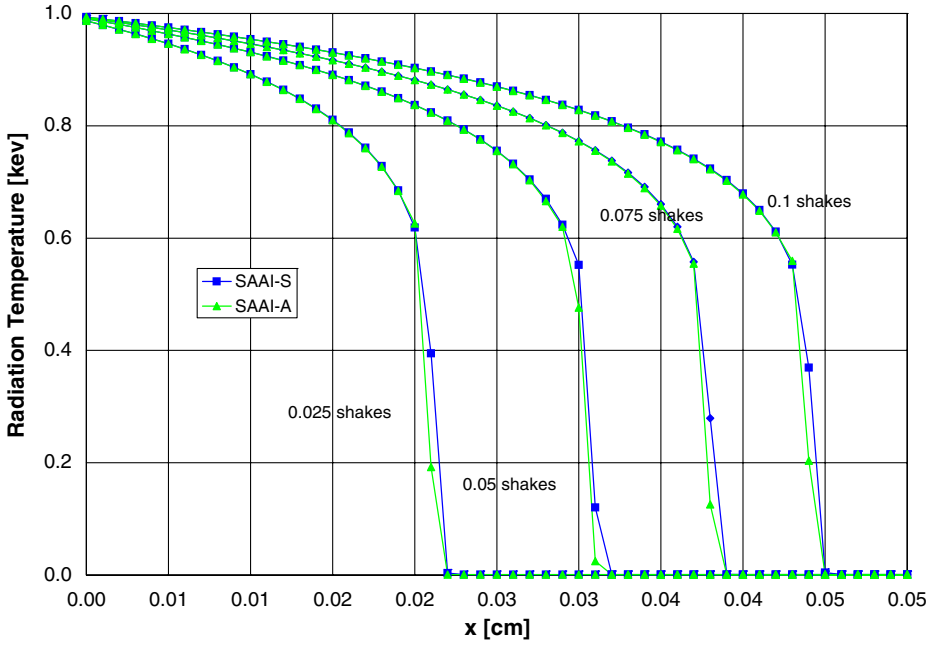

Fig. 4. Comparison of the standard and alternative SAAI discretizations with 50 spatial cells.

reduced material heating. The steady-state material temperature solutions for the standard and alternative SAAI discretizations in the region of the interfaces are illustrated in Fig. 5. It can be seen from Fig. 5 that the alternative scheme solution oscillates at the interfaces, while the standard scheme solution does not. Even if the calculation is performed again using the standard scheme with half as many cells, the solution does not

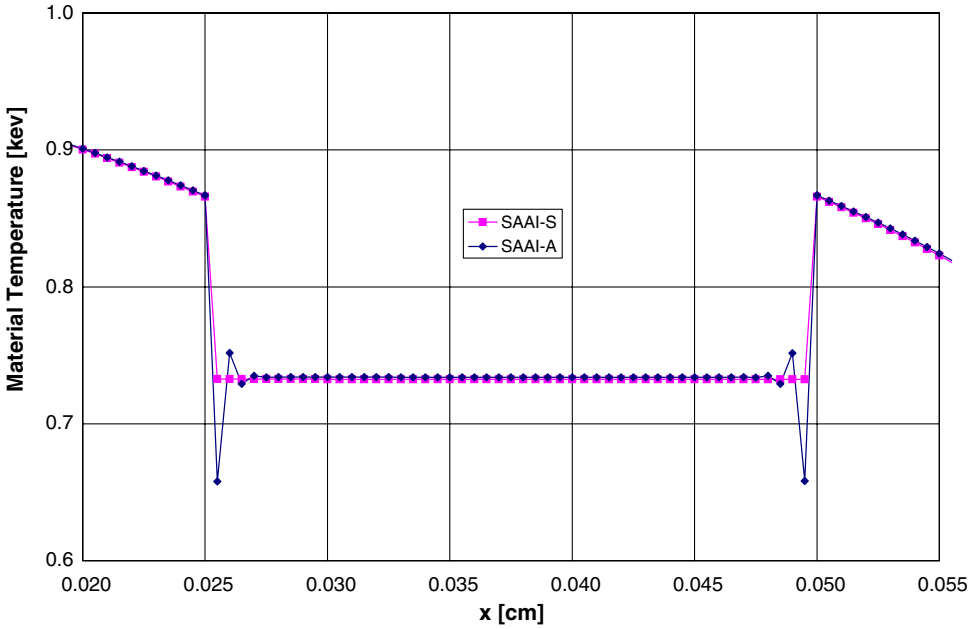

Fig. 5. Standard and alternative SAAI temperatures with large material opacity discontinuities.

oscillate. Thus, we have found one example problem for which the standard scheme is more robust than the alternative scheme. We have not found any counter-examples.

9.2. Two-dimensional results

The fifth and final set of calculations was performed to demonstrate the effectiveness of our alternative SAAI discretizations in multi-dimensional geometry. The test problem that we selected is a 2-D Cartesian geometry version of the 1-D Marshak wave problem discussed in the previous section. The upper half of the Cartesian problem geometry and the computational mesh are illustrated in Fig. 6. The bottom edge of the mesh represents the centerline of the problem geometry; the "inlet" of the problem geometry is on the left side and has coordinates of $x = 0.0$ cm and $0.0 \leqslant y \leqslant 0.0075$ cm; the "outlet" located on the right edge of the mesh has coordinates of $x = 0.05$ cm and $0.0 \leqslant y \leqslant 0.0075$ cm. An optically-thin region is located adjacent to the problem centerline and has vertical coordinates of $0.0 \leqslant y \leqslant 0.0025$ cm; an optically-thick region occupies the remaining area located between $0.0025 \leqslant y \leqslant 0.0075$ cm. The optically-thick region has material properties identical to those previously used for the 1-D Marshak wave problem; the temperature-dependent macroscopic absorption cross-section is again given by $\sigma_a = 300/(T^3)$ cm^{-1} with T in keV, and the constant heat capacity has a value of 0.3 $\frac{\text{Jks}}{\text{cm}^3-\text{keV}}$. The material properties for the optically-thin region were simply taken as a factor of ten lower than these values; the macroscopic absorption cross-section is given by $\sigma_a = 30/(T^3)$ cm^{-1}, and the heat capacity has a value of 0.03 $\frac{\text{Jks}}{\text{cm}^3-\text{keV}}$. The scattering cross-section is everywhere zero. An isotropic angular intensity with a black-body temperature of 1.0 keV is incident at the problem inlet. This source intensity is constant along the entire length of the inlet and is constant in time. All points in the problem have an initial material temperature of 0.001 keV and a corresponding initial black-body radiation intensity. In addition to satisfying a source condition along the inlet, the radiation intensity satisfies a reflective boundary condition along the bottom face of the mesh, and a vacuum condition at all other boundary points. The computational mesh has a total of 3300 spatial cells. There are 100 zones of uniform width in x from $x = 0.0$ cm to $x = 0.0475$ cm. There are 10 zones in x between $x = 0.0475$ cm and $x = 0.05$ cm that logarithmically decrease to a minimum cell width of 10^{-4} cm. There are 10 zones in y between $y = 0.0$ cm and $y = 0.0025$ cm that logarithmically decrease to a minimum cell width of 10^{-4} cm. There are 10 zones in y between $y = 0.0025$ cm and $y = 0.0050$ cm that logarithmically increase from minimum cell width of 10^{-4} cm. Finally, there are 10 zones in y between $y = 0.0050$ cm and $y = 0.0075$ cm that logarithmically decrease to a minimum cell width of 10^{-4} cm.

We performed S_{16} calculations for this problem using the alternative SAAI discretization. All of these calculations were performed using parity-equivalent source and vacuum boundary conditions together with the non-essential reflective boundary condition defined in Eqs. (A.35) and (A.36). To obtain a reference solution, a calculation for this problem was performed using the standard Implicit Monte-Carlo method [23]. Based upon preliminary calculations, a fixed time step of $\Delta t = 1 \times 10^{-6}$ shakes (1×10^{-8} s/shake) was used in all calculations. It can be seen from Fig. 6 that highly refined mesh spacing is used along the entire interface between the optically-thin and optically-thick materials. As one would expect, preliminary calculations indicated that such meshing is necessary to obtain an accurate solution for both the S_n and Monte-Carlo methods. We also elected

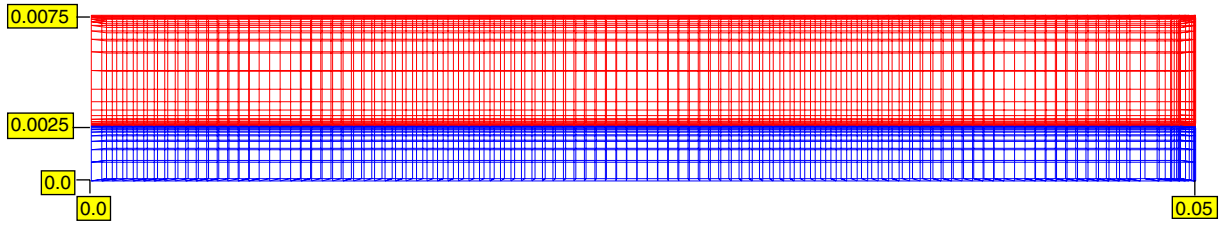

Fig. 6. Two-dimensional Marshak geometry and meshing. Dimensions are in centimeters. The left-bottom corner of the mesh corresponds to the origin of the Cartesian coordinate system. The x-axis is located along the bottom edge of the geometry, and the y-axis is located along the left edge of the geometry.

to apply refined zoning at the vacuum boundaries to minimize negativities that were observed in the SAAI solution at these interfaces.

Contour plots of the S_n radiation temperature solutions at times of 5×10^{-4}, 1×10^{-2}, and 2×10^{-2} shakes are shown in Fig. 7. These plots are provided herein to allow a qualitative assessment of the wave behaviour – they are not particularly useful for quantitative analysis. We provide a detailed quantitative analysis in subsequent comparisons to the Monte-Carlo method results. It should be noted that the vertex radiation temperatures are plotted in the figures since all calculated quantities are vertex-based in our alternative SAAI spatial discretization scheme. As to be expected, the wave travels faster in the optically-thin region than in the optically-thick region due to the reduced opacity in this portion of the problem. The highest wave velocity occurs at the problem centerline, as some of the initial source energy within the optically-thin region is lost to material heating at the interface with the optically-thick region. The slowest wave speed occurs at the vacuum boundary located along the top edge of the mesh, since energy is simply radiated to space at this interface. The retarding influence of the optically-thick region on the wave speed within the optically-thin region can be verified by comparing the two-dimensional radiation profiles in Fig. 7 with the one-dimensional profiles that were previously shown for the Marshak wave problem in Figs. 1, 3, and 4 of the proceeding subsection. The 1-D, time-dependent, temperature distribution plots are provided at slightly different problem times so again a direct quantitative comparison is not possible, but it can be noted that the 1-D results predict both a sharper gradient at the wavefront and larger material temperatures than is noted for the optically-thin regions in the 2-D solutions.

The computed radiation temperature distributions obtained with both our alternative SAAI discretization scheme and the IMC code are given in Fig. 8 at a time of 0.02 shakes. To allow a direct comparison with cell-centered IMC results we provided an option within our SAAI code to calculate cell-centered intensities and temperatures using a simple average. The SAAI cell-centered temperatures are displayed in Fig. 9. We elected to compare the discrete and stochastic results in the first row of cells adjacent to the centerline, and in the two rows of cells adjacent to the middle of the optically-thick region which lies along a row of vertices (i.e., $y = 0.005$ cm). Referring to the figure, excellent agreement is obtained for the radiation temperatures predicted with the two methods. With the exception of the statistical variation inherent in the Monte-Carlo method the

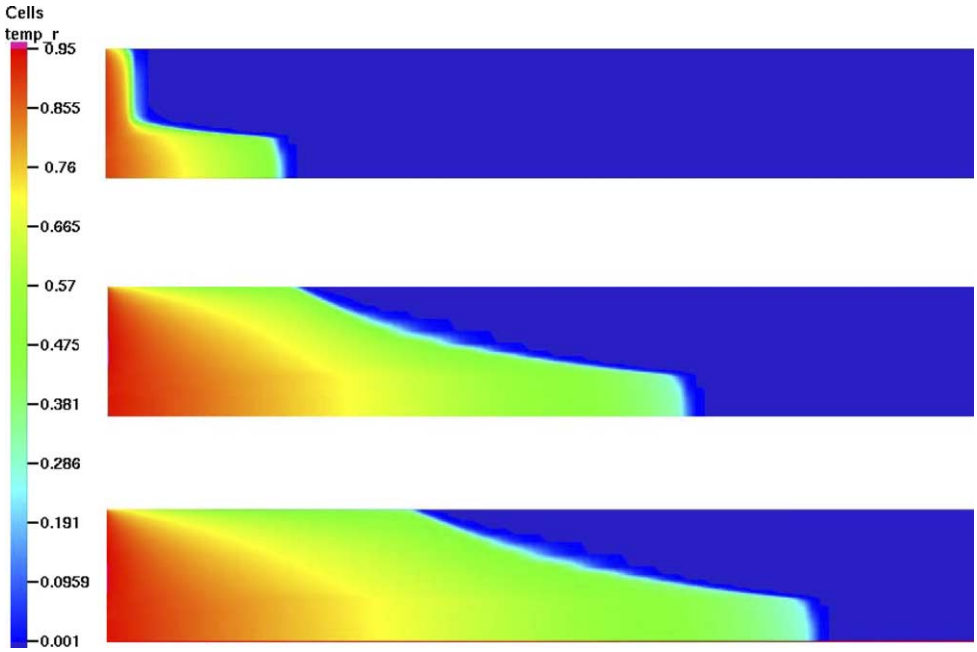

Fig. 7. SAAI radiation temperature profiles at 5×10^{-4}, 1×10^{-2}, and 2×10^{-2} shakes.

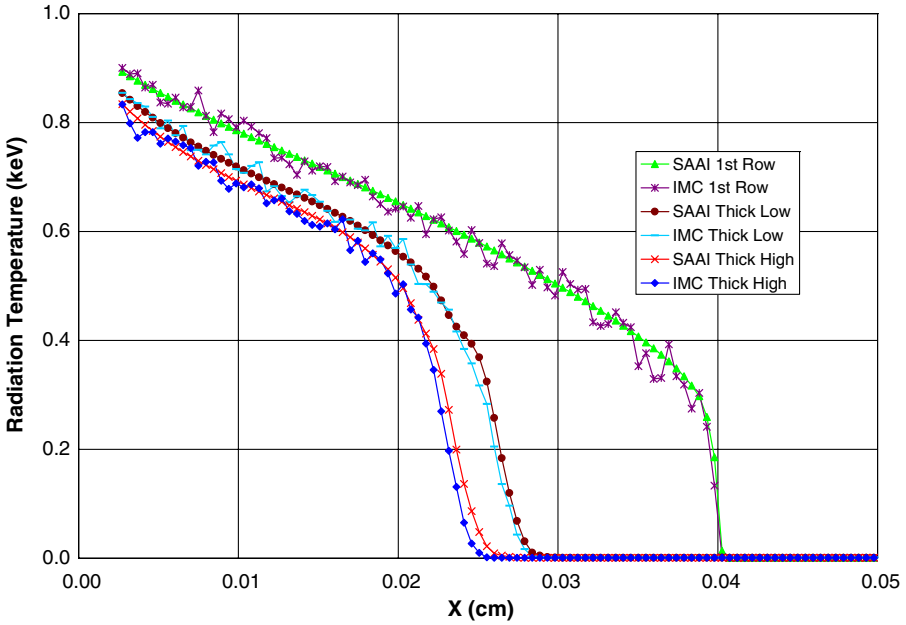

Fig. 8. Cell radiation temperature profiles at 2×10^{-2} shakes. "1st Row" refers to the first row of cells located above the center-line. "Thick Low" and "Thick High" refer to the rows of cells located below and above, respectively, the mid-point of the optically-thick region (i.e., $y = 0.005$ cm).

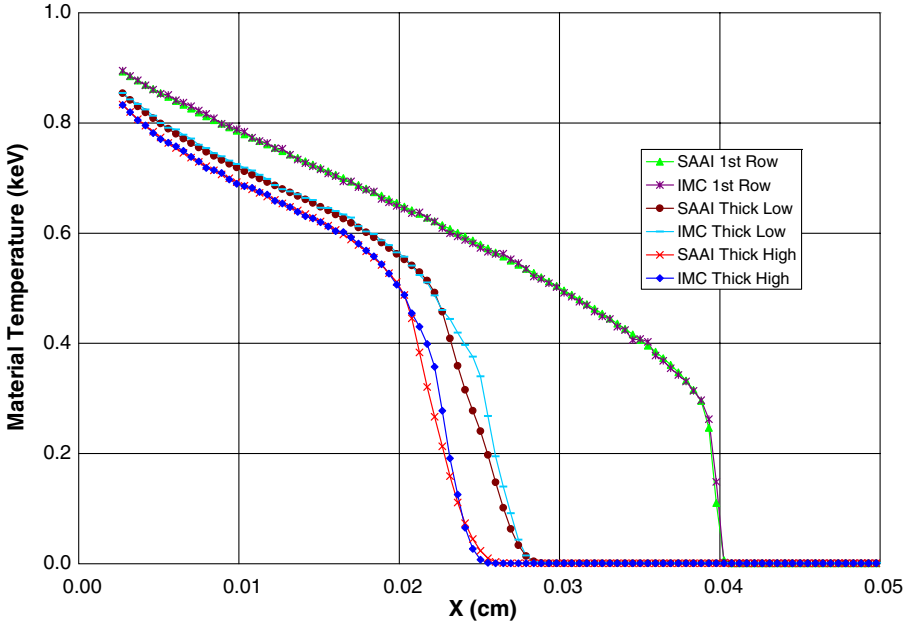

Fig. 9. Cell material temperature profiles at 2×10^{-2} shakes. "1st Row" refers to the first row of cells located above the center-line. "Thick Low" and "Thick High" refer to the rows of cells located below and above, respectively, the mid-point of the optically-thick region (i.e., $y = 0.005$ cm).

results are identical along the problem center-line. The radiation temperatures predicted with our alternative SAAI scheme lead the IMC method along the midpoint of the optically-thick region, although the effect is quite small. This small discrepancy is eliminated after the wave front has passed, and the two codes predict

the same equilibrated radiation temperatures. Although not reported herein, we initially performed the 2-D Marshak wave discrete ordinates calculations using S_4 angular quadrature. This low-order quadrature did not have sufficient angular resolution to transport radiation in a horizontal direction through the problem geometry. The S_4 calculations thus showed our alternative SAAI discretization results lagging those of the IMC code significantly. This effect was eliminated with the higher-order S_{16} angular quadrature. This is in stark contrast to our one-dimensional Marshak wave calculation results where S_2 quadrature was found to be fully adequate. Our two-dimensional Marshak wave problem introduces an additional angular dependence that is not present in the one-dimensional case.

The cell material temperatures predicted by our SAAI alternative discretization scheme and the Monte-Carlo technique are provided in Fig. 9. Again, the vertex-based calculated material temperatures were averaged to output a cell-center quantity that can be compared directly with the IMC results. The agreement between the two codes is actually improved relative to those obtained for the radiation temperatures previously illustrated in Fig. 8. Some of this noted improvement is due to the IMC material temperature solution exhibiting significantly less statistical fluctuation. The material temperatures predicted along the problem center-line are again virtually identical. Referring to Fig. 9 and comparing the code predictions along the middle of the optically-thick region, the IMC results lead our SAAI temperatures at the wave front. This is the opposite behaviour of that observed for the radiation temperatures. The IMC code calculates the material temperatures in a non-linearly explicit manner, while our SAAI code utilizes Newton iteration to converge the material temperature value. This fact might influence the very slight discrepancy that is observed in the results. Both codes predict the same final, equilibrated material temperatures.

10. Conclusions

A general, arbitrary-order, continuous spatial finite-element discretization scheme has been developed for the self-adjoint forms of the radiative transfer equations: the even-parity equations, the odd-parity equations, and the self-adjoint angular intensity equations. An alternative spatial discretization scheme unique to the SAAI equations has also been presented. While we have limited our discussion to the S_n discrete ordinates method, our scheme is equally applicable to the P_n spherical-harmonics method.

We have computationally tested both our standard and alternative SAAI finite-element spatial discretization schemes in one-dimensional Cartesian geometry. The alternative scheme exhibited slightly less robustness than the standard scheme in a 1-D problem with severely discontinuous material properties, but the alternative scheme exhibited reasonably good robustness in all the other calculations that were performed. We have developed a prototype modification to the algorithm to better treat severe material discontinuities that should be further investigated in the future. As previously discussed, the alternative scheme requires far less memory than the standard scheme, because the alternative scheme has unknowns only at the vertices, whereas the standard scheme has unknowns at both the vertices and the spatial quadrature points. If one considers only vertex solutions, the alternative and standard schemes appear to have comparable accuracy. However, the standard scheme gives anomalously accurate results when the solution at the vertices is averaged over the cell with the solution at the spatial quadrature points. Nonetheless, it seems clear that the alternative scheme is useful and attractive due to its low memory requirements. Much more practical experience with the standard and alternative schemes will be required to determine all of their relative advantages and disadvantages for various classes of problems. In the future, the relative performance of these two schemes with high-order trial spaces should be investigated because the advantage in memory usage associated with the alternative scheme rapidly increases with the order of the trial space. Our computational results for the two-dimensional Marshak wave problem are very encouraging and clearly indicate that our self-adjoint methods are extendable to multi-dimensional and multi-material problems.

In the process of determining adequate zoning for a wide variety of problems, we have found our lumped continuous finite-element methods somewhat more sensitive to the spatial meshing than one would expect based upon experience with such methods in diffusion calculations. We suspect that this degraded robustness follows from the fact that diffusion solutions are generally quite smooth, while discontinuities in the angular intensity and/or its derivatives are easily introduced into the transport solution by spatially localized sources and geometric shadowing. The accuracy of all discretization techniques will be degraded by discontinuities

unless they are specifically designed to capture them, but we suspect that continuous finite-element techniques are particularly sensitive because they cannot capture discontinuities in the solution at cell interfaces. Thus, one must be particularly cautious when applying the finite-element schemes described in this paper to problems with strong solution discontinuities. If one is aware of the presence of solution discontinuities, one can often mitigate their severity by slightly modifying the problem definition. For instance, one can replace spatially discontinuous sources with localized smooth sources. The use of higher-order continuous finite-element spatial discretizations should be examined in the future to see how robustness is affected. One would generally expect higher-order methods to be even less robust than lower-order methods, but good results for multidimensional coupled electron–photon transport calculations have been obtained with continuous quadratic spatial elements [14,16].

Discretizations for second-order operators can be generally expected to be more numerically diffusive than discretizations for first-order operators. This deficiency is exacerbated in problems that are extremely optically thin. Furthermore, difficulties can arise in time-dependent problems with solution modes that fail to attenuate in time or attenuate far too slowly. Such modes are associated with the null space of the steady-state operator, and arise entirely due to discretization effects. Gesh and Adams [20] discuss such modes in detail for discretizations of the odd-parity equation. A useful alternative in near-void calculations might be to first compute the uncollided intensity component (uncollided from the start of each time step) using a Monte-Carlo or integral transport technique, and then compute the collided intensity component using a self-adjoint form of the transport equation. We have produced a lengthy report in which self-adjoint forms of the radiative transfer equations are applied to a wide variety of problems including those with near voids [27]. Regardless of inherent limitations associated with the solution of self-adjoint forms of the radiative transfer equations, it is clear from our results that there are many classes of problems for which these equations may be used to obtain accurate transport solutions. We conclude from our results that self-adjoint forms of radiative transfer equations represent a useful alternative to traditional first-order forms, and that self-adjoint forms are worthy of further study.

Acknowledgments

We thank Dr. Paul Batcho for performing the one-dimensional Marshak wave calculations using his first-order radiative transport code. Los Alamos National Laboratory is operated by the University of California for the United State Department of Energy under contract W-7405-ENG-36.

Appendix A

The purpose of this appendix is to derive source and reflective boundary conditions for the even-parity, odd-parity, and SAAI equations with S_n angular discretization. The vacuum condition is a special case of the source condition. Specifically, a source condition with an incident intensity of zero is equivalent to a vacuum condition. Thus, we do not explicitly derive vacuum conditions. Source conditions are straightforward for all of the equations and are really independent of the angular discretization. Unfortunately, this is not the case for reflective boundary conditions.

Eqs. (51), (57), (59), and (71), which are associated with the even-parity discretization, the odd-parity discretization, the standard SAAI discretization, and the alternative SAAI discretization, respectively, are the only equations that depend upon the boundary conditions. In particular, the surface integral term in each of these equations has a form particular to the vacuum boundary condition. To facilitate a description of the various boundary conditions we replace these specific forms with non-specific generic forms. Specifically, Eq. (51) becomes

$$\oint_{\delta V} \beta_g \psi_s^- \vec{\Omega}\cdot\vec{n}\,\mathrm{d}A - \sum_{n=1}^{N_g}\sum_{j=1}^{D_{\mathbf{k}}}\left\{\left[-\frac{1}{\sigma_\tau}\vec{\Omega}\cdot\left(\vec{\nabla}\tilde{\psi}^+\right)_{\mathbf{k},j} + \frac{Q^-_{\mathbf{k},j}}{\sigma_\tau}\right]\vec{\Omega}\cdot\left(\vec{\nabla}\gamma_{\mathbf{k},\mathbf{i}}\right)_{\mathbf{k},j}\right\} w_{\mathbf{k},j} + \int_V \beta_g[\sigma_\tau\tilde{\psi}^+ - \tilde{Q}^+]\,\mathrm{d}V = 0, \tag{A.1}$$

Eq. (57) becomes

$$\oint_{\delta V} \beta_g \psi_s^+ \vec{\Omega}\cdot\vec{n}\,\mathrm{d}A - \sum_{n=1}^{N_g}\sum_{j=1}^{D_{\mathbf{k}}}\left\{\left[-\frac{1}{\sigma_\tau}\vec{\Omega}\cdot(\vec{\nabla}\tilde{\psi}^-)_{\mathbf{k},j} + \frac{Q^+_{\mathbf{k},j}}{\sigma_\tau}\right]\vec{\Omega}\cdot(\vec{\nabla}\gamma_{\mathbf{k},\mathbf{i}})_{\mathbf{k},j}\right\} w_{\mathbf{k},j} + \int_V \beta_g[\sigma_\tau\tilde{\psi}^- - \widetilde{Q}^-]\,\mathrm{d}V = 0, \tag{A.2}$$

Eq. (59) becomes

$$\oint_{\delta V} \beta_g \psi_s \vec{\Omega}\cdot\vec{n}\,\mathrm{d}A - \sum_{n=1}^{N_g}\sum_{j=1}^{D_{\mathbf{k}}}\left\{\left[-\frac{1}{\sigma_\tau}\vec{\Omega}\cdot(\vec{\nabla}\tilde{\psi})_{\mathbf{k},j} + \frac{Q_{\mathbf{k},j}}{\sigma_\tau}\right]\vec{\Omega}\cdot(\vec{\nabla}\gamma_{\mathbf{k},\mathbf{i}})_{\mathbf{k},j}\right\} w_{\mathbf{k},j} + \int_V \beta_g[\sigma_\tau\tilde{\psi} - \widetilde{Q}]\,\mathrm{d}V = 0, \tag{A.3}$$

and Eq. (71) becomes

$$\oint_{\delta V} \beta_g \psi_s \vec{\Omega}\cdot\vec{n}\,\mathrm{d}A - \int_V \left[-\frac{1}{\sigma_\tau}\vec{\Omega}\cdot\vec{\nabla}\tilde{\psi} + \frac{\widetilde{Q}}{\sigma_\tau}\right]\vec{\Omega}\cdot\vec{\nabla}\beta_g\,\mathrm{d}V + \int_V \beta_g[\sigma_\tau\tilde{\psi} - \widetilde{Q}]\,\mathrm{d}V = 0, \tag{A.4}$$

where ψ_s^-, ψ_s^+, and ψ_s denote the odd-parity, even-parity, and self-adjoint angular intensities defined on the outer boundary of the mesh. We stress that these are to be considered independent unknowns that must be defined in terms of the trial-space unknowns via the boundary conditions.

A.1. Even-parity source condition

We first consider the source condition for the even-parity equation. Our task is to define a relationship between the even-parity angular intensity and the odd-parity angular intensity on the source boundary surface, and then use that relationship to define ψ_s^- in Eq. (A.1) in terms of the trial-space representation for ψ^+. At a vacuum boundary, the angular intensity physically satisfies

$$\psi(\vec{\Omega}) = f(\vec{\Omega}) \quad \text{for } \vec{\Omega}\cdot\vec{n} < 0, \tag{A.5}$$

where $f(\vec{\Omega})$ is the "boundary source function" that specifies the incoming angular intensity. Adding Eqs. (7) and (8), we obtain

$$\psi(\vec{\Omega}) = \psi^+(\vec{\Omega}) + \psi^-(\vec{\Omega}). \tag{A.6}$$

Substituting from Eq. (A.6) into Eq. (A.5), we get

$$\psi^+(\vec{\Omega}) + \psi^-(\vec{\Omega}) = f(\vec{\Omega}) \quad \text{for } \vec{\Omega}\cdot\vec{n} < 0. \tag{A.7}$$

Solving Eq. (A.7) for ψ^-, we get

$$\psi^-(\vec{\Omega}) = -\psi^+(\vec{\Omega}) + f(\vec{\Omega}) \quad \text{for } \vec{\Omega}\cdot\vec{n} < 0. \tag{A.8}$$

To obtain a similar relationship for $\vec{\Omega}\cdot\vec{n} > 0$, we note that Eq. (A.5) implies that

$$\psi(-\vec{\Omega}) = f(-\vec{\Omega}) \quad \text{for } \vec{\Omega}\cdot\vec{n} > 0. \tag{A.9}$$

Manipulating Eq. (A.9) in analogy with the manipulation of Eq. (A.5), we obtain

$$\psi^-(\vec{\Omega}) = \psi^+(\vec{\Omega}) - f(\vec{\Omega}) \quad \text{for } \vec{\Omega}\cdot\vec{n} > 0. \tag{A.10}$$

Eqs. (A.8) and (A.10) constitute the desired relationships. Using them to define ψ_s^-, we obtain:

$$\psi_s^-(\vec{\Omega}) = -\tilde{\psi}^+(\vec{\Omega}) + f(\vec{\Omega}) \quad \text{for } \vec{\Omega}\cdot\vec{n} < 0, \tag{A.11}$$

$$\psi_s^-(\vec{\Omega}) = \tilde{\psi}^+(\vec{\Omega}) - f(\vec{\Omega}) \quad \text{for } \vec{\Omega}\cdot\vec{n} > 0, \tag{A.12}$$

where $\tilde{\psi}^+$ denotes the even-parity trial-space intensity on the boundary surface.

A.2. Odd-parity source condition

We next consider source boundary conditions for the odd-parity equation. The relationships that are used to express ψ^- in terms of ψ^+ on a source boundary can also be used to express ψ^+ in terms of ψ^-. In particular,

re-expressing Eqs. (A.8) and (A.10) for this task, we, respectively, get the relationships use them to define ψ_s^+ in Eq. (A.2) in terms of the trial-space representation for ψ^-:

$$\psi_s^+(\vec{\Omega}) = -\tilde{\psi}^-(\vec{\Omega}) + f(\vec{\Omega}) \quad \text{for } \vec{\Omega}\cdot\vec{n} < 0, \tag{A.13}$$

$$\psi_s^+(\vec{\Omega}) = \tilde{\psi}^-(\vec{\Omega}) + f(\vec{\Omega}) \quad \text{for } \vec{\Omega}\cdot\vec{n} > 0. \tag{A.14}$$

A.3. SAAI source conditions

There are several possible source boundary condition treatments for the SAAI equation. First, we derive a treatment directly from those for the even-parity and odd-parity equations. In particular, summing Eqs. (A.11) and (A.13), we obtain

$$\psi_s(\vec{\Omega}) = -\tilde{\psi}(\vec{\Omega}) + 2f(\vec{\Omega}) \quad \text{for } \vec{\Omega}\cdot\vec{n} < 0. \tag{A.15}$$

Summing Eqs. (A.12) and (A.14), we obtain

$$\psi_s(\vec{\Omega}) = \tilde{\psi}(\vec{\Omega}) \quad \text{for } \vec{\Omega}\cdot\vec{n} > 0. \tag{A.16}$$

We refer to these as the parity-equivalent source conditions because they make the solution of the SAAI equation with the standard discretization equivalent to the simultaneous solution of the even-parity and odd-parity equations with the standard discretization and standard source boundary conditions. These boundary conditions were originally derived for the SAAF neutron transport equation by Gesh and Adams [21]. Eq. (A.15) is certainly of a non-intuitive nature. More physically intuitive boundary conditions exist, but they do not result in parity equivalence.

In particular, the SAAI source conditions given in [2] are much more physically-intuitive than the parity-equivalent conditions because ψ_s is simply equal to f for the incoming directions:

$$\psi_s(\vec{\Omega}) = f(\vec{\Omega}) \quad \text{for } \vec{\Omega}\cdot\vec{n} < 0, \tag{A.17}$$

$$\psi_s(\vec{\Omega}) = \tilde{\psi}(\vec{\Omega}) \quad \text{for } \vec{\Omega}\cdot\vec{n} > 0. \tag{A.18}$$

The non-intuitive nature of the parity-equivalent boundary conditions makes it unclear as to whether these conditions are conservative. They are indeed conservative, but the radiation energy leakage from the system must be calculated in a specific manner. In particular, the net leakage is first calculated in the usual way

$$\vec{F}\cdot\vec{n} = \int_{4\pi} \tilde{\psi}(\vec{\Omega})\vec{\Omega}\cdot\vec{n}\,\mathrm{d}\Omega, \tag{A.19}$$

where $\vec{F}\cdot\vec{n}$ denotes the net leakage. The inflow, denoted by f_{in}, is next calculated using $f(\vec{\Omega})$ rather than the trial-space solution

$$f_{\text{in}} = -\int_{\vec{\Omega}\cdot\vec{n}<0} f(\vec{\Omega})\vec{\Omega}\cdot\vec{n}\,\mathrm{d}\Omega. \tag{A.20}$$

Finally, the outflow, denoted by f_{out} is calculated by adding the inflow to the net leakage

$$f_{\text{out}} = \int_{4\pi} \tilde{\psi}(\vec{\Omega})\vec{\Omega}\cdot\vec{n}\,\mathrm{d}\Omega + \int_{\vec{\Omega}\cdot\vec{n}<0} f(\vec{\Omega})\vec{\Omega}\cdot\vec{n}\,\mathrm{d}\Omega. \tag{A.21}$$

Note that if the incoming values of $\tilde{\psi}(\vec{\Omega})$ are not equal to $f(\vec{\Omega})$, the incoming values of $\tilde{\psi}$ contribute to the outflow. This is clearly non-physical. However, the contribution to the outflow from the inflow directions approaches zero as the mesh is refined.

A.4. Reflective conditions

In general, reflective boundary conditions are more difficult to implement than source conditions because they are essential boundary conditions, i.e., the trial-space must be forced to exactly satisfy these conditions. There are two caveats to this statement. First, in 1-D slab calculations, the reflective condition is a natural

rather than essential condition. Second, one can implement a reflective condition for the SAAF equation that is not essential, but it generates an asymmetric directional coupling. This is not a problem if the S_n equations are solved using the standard S_n source iteration technique, because the asymmetry does not appear in the coefficient matrices for the iteration equations. Our symmetric implementation of the reflective boundary condition is essentially identical for the even-parity, odd-parity, and SAAI equations.

We do not consider reflective conditions on arbitrary surfaces or arbitrarily-oriented flat surfaces, but rather only on flat surfaces that are parallel to a coordinate plane, i.e., parallel to the $x-y$, $y-z$, or $x-z$ planes. We refer to such surfaces as coordinate surfaces. This limitation is required for S_n calculations because standard S_n quadrature directions are symmetric only with respect to coordinate surfaces. This restriction is not serious since reflective boundary conditions are usually imposed only to reduce the size of the computational domain in problems with some degree of symmetry about one or more orthogonal planes. If such planes are not parallel to coordinate surfaces, they can generally be made so via rotation of the coordinate axes.

A.4.1. Even-parity reflective condition

On a reflective surface, the angular intensity physically satisfies

$$\psi(\vec{\Omega}) = \psi(\vec{\Omega}') \quad \text{for all } \vec{\Omega}\cdot\vec{n} < 0, \tag{A.22}$$

where $\vec{\Omega}'$ is the mirror image of $\vec{\Omega}$ relative to the reflective surface, i.e.,

$$\vec{\Omega}\cdot\vec{n} = -\vec{\Omega}'\cdot\vec{n} \tag{A.23}$$

and

$$\vec{\Omega}\times\vec{n} = \vec{\Omega}'\times\vec{n}. \tag{A.24}$$

We next manipulate Eq. (A.22) to obtain relationships for the even-parity and odd-parity intensities on a reflective surface. In particular, substituting from Eq. (A.6) into Eq.(A.22), we get

$$\psi^+(\vec{\Omega}) + \psi^-(\vec{\Omega}) = \psi^+(\vec{\Omega}') + \psi^-(\vec{\Omega}') \quad \text{for all } \vec{\Omega}\cdot\vec{n} < 0. \tag{A.25}$$

Substituting $-\vec{\Omega}'$ for $\vec{\Omega}$ in Eq. (A.25), we obtain

$$\psi^+(-\vec{\Omega}') + \psi^-(-\vec{\Omega}') = \psi^+(-\vec{\Omega}) + \psi^-(-\vec{\Omega}) \quad \text{for all } -\vec{\Omega}'\cdot\vec{n} < 0. \tag{A.26}$$

Using Eqs. (7) and (8), it follows from Eq. (A.25) that

$$\psi^+(\vec{\Omega}') - \psi^-(\vec{\Omega}) = \psi^+(\vec{\Omega}) - \psi^-(\vec{\Omega}) \quad \text{for all } \vec{\Omega}'\cdot\vec{n} > 0. \tag{A.27}$$

By adding Eqs. (A.25) and (A.27), we find that

$$\psi^+(\vec{\Omega}) = \psi^+(\vec{\Omega}') \quad \text{for all } \vec{\Omega} \tag{A.28}$$

and by subtracting Eq. (A.27) from Eq. (A.25), we find that

$$\psi^-(\vec{\Omega}) = \psi^-(\vec{\Omega}') \quad \text{for all } \vec{\Omega}. \tag{A.29}$$

Eqs. (A.28) and (A.29) are the basis of reflective boundary treatments for both the even-parity and odd-parity equations. However, we cannot proceed in analogy with the source treatments because Eqs. (A.28) and (A.29) do not relate ψ^+ and ψ^- on a reflective boundary. Thus we cannot directly use these equations to define ψ_s^- in Eq. (A.1) in terms of the ψ^+. Nonetheless, we can use these equations together with algebraic manipulation of the equations for $\psi^+(\vec{\Omega})$ and $\psi^+(\vec{\Omega}')$ to obtain new equations for $\psi^+(\vec{\Omega})$ and $\psi^+(\vec{\Omega}')$ that do not contain the odd-parity intensity. In particular, if we average the equations for $\psi^+(\vec{\Omega})$ and $\psi^+(\vec{\Omega}')$, it follows from Eqs. (A.23) and (A.29) that the surface terms containing $\psi_s^-(\vec{\Omega})$ and $\psi_s^-(\vec{\Omega}')$ will cancel, thereby eliminating these odd-parity intensities from the resulting equation. We can then use Eq. (A.28) together with this average equation to obtain a new equation for $\psi^+(\vec{\Omega})$ and a new equation for $\psi^+(\vec{\Omega}')$. However, in practice we must ensure that these new equations are cast in such a way that there is no singularity or asymmetry associated with them.

To this end, we define the following implementation algorithm for the case of S_n angular discretization. Let $C_{k,j}$ denote the coefficient matrix element associated with unknown j in the equation for unknown k. Further,

let i denote the index for $\psi^+(\vec{\Omega})$ and let i' denote the index for $\psi^+(\vec{\Omega}')$. To implement the reflective boundary conditions for $\psi^+(\vec{\Omega})$ and $\psi^+(\vec{\Omega}')$:

1. Initially generate the equations for $\psi^+(\vec{\Omega})$ and $\psi^+(\vec{\Omega}')$ with the boundary surface term set to zero.
2. Next average the equations for $\psi^+(\vec{\Omega})$ and $\psi^+(\vec{\Omega}')$

$$C_{i,j}^{(1)} = C_{i',j}^{(1)} = \frac{1}{2}\left[C_{i,j}^{(0)} + C_{i',j}^{(0)}\right] \quad \text{for all } j, \tag{A.30}$$

   where $C_{i,j}^{(n)}$ denotes the coefficient $C_{i,j}$ after the nth algorithmic step. At this point, the matrix is singular because two rows are identical.
3. Remove the singularity by first adding the off-diagonal coefficient associated with $\psi^+(\vec{\Omega}')$ in the equation for $\psi^+(\vec{\Omega})$ to the diagonal, then adding the off-diagonal coefficient associated with $\psi^+(\vec{\Omega})$ in the equation for $\psi^+(\vec{\Omega}')$ to the diagonal, and then set the original off-diagonal coefficient to zero in both equations:

$$C_{i,i}^{(2)} = C_{i,i}^{(1)} + C_{i,i'}^{(1)}, \tag{A.31}$$

$$C_{i',i'}^{(2)} = C_{i',i'}^{(1)} + C_{i',i}^{(1)}, \tag{A.32}$$

$$C_{i,i'}^{(2)} = C_{i',i}^{(2)} = 0. \tag{A.33}$$

4. Restore symmetry to the system by averaging the off-diagonal coefficients associated with $\psi^+(\vec{\Omega})$ and $\psi^+(\vec{\Omega}')$ in all equations other than those for $\psi^+(\vec{\Omega})$ and $\psi^+(\vec{\Omega}')$

$$C_{j,i}^{(3)} = C_{j,i'}^{(3)} = \frac{1}{2}\left[C_{j,i}^{(2)} + C_{j,i'}^{(2)}\right] \quad \text{for all } j \text{ not equal to } i \text{ or } i'. \tag{A.34}$$

There are three complications that can arise with this process, and they can be dealt with as described below:

1. Because the angular domain for the even-parity equation is half the unit sphere, $\vec{\Omega}$ can be in the angular domain when $\vec{\Omega}'$ is not in the angular domain. In this case, the equation for $\psi^+(\vec{\Omega})$ should be averaged with the equation for $\psi^+(-\vec{\Omega}')$. This follows for three reasons. First, $-\vec{\Omega}'$ will always be in the angular domain if $\vec{\Omega}$ is not, second, $\psi^+(-\vec{\Omega}') = \psi^+(\vec{\Omega}')$, and third, $-\vec{\Omega}' \cdot \vec{n}\psi^-(-\vec{\Omega}') = \vec{\Omega}' \cdot \vec{n}\psi^-(\vec{\Omega}')$.
2. A vertex can be shared by two reflective surfaces (a reflective edge vertex). In this case, one must average the four equations associated with $\vec{\Omega}$, $\vec{\Omega}'$, $\vec{\Omega}''$, and $\vec{\Omega}'''$, where $\vec{\Omega}$ and $\vec{\Omega}'$ are mirror images with respect to the "first" reflective surface (arbitrarily chosen), $\vec{\Omega}''$ is the mirror image of $\vec{\Omega}'$ with respect to the second reflective surface, and $\vec{\Omega}'''$ is both the mirror image of $\vec{\Omega}''$ with respect to the first reflective surface and the mirror image of $\vec{\Omega}$ with respect to the second reflective surface.
3. A vertex can be shared by three reflective coordinate surfaces (a reflective corner vertex.) In this case, no averaging is required because $\psi^-(\vec{\Omega})$ is identically zero at a reflective corner for all $\vec{\Omega}$.

Various combinations of these complications can arise, e.g. two of the four intensities that need to be averaged at a vertex shared by two reflective surfaces may not be in the trial-space. We do not explicitly address these combinations. They are dealt with by appropriately combining the various procedures described above.

Overall, this is very complex algorithm. Its implementation is facilitated by carrying out the process at the element level when assembling the coefficient matrix rather than carrying it out after the coefficient matrix has been assembled. Nonetheless, we consider the implementation of these boundary conditions to be sufficiently onerous to discourage the use of reflective boundary conditions with the even-parity S_n equations.

A.4.2. Odd-parity reflective conditions

Implementation of reflective boundary conditions for the odd-parity equations with S_n angular discretization is almost completely analogous to that for the even-parity equations. The only exception relates to the

case where $\psi^-(\vec{\Omega})$ is in the angular domain, but $\psi^-(\vec{\Omega}')$ is not. In this case, $-\psi^-(-\vec{\Omega}') = \psi^-(\vec{\Omega})$, so the two unknowns are not equal to each other, but rather equal in magnitude and opposite in sign. To eliminate the surface leakage terms in the equations for these unknowns, their equations must be subtracted rather than added.

A.4.3. SAAI parity-equivalent reflective conditions

The implementation of parity-equivalent reflective boundary conditions for the SAAI equation with S_n angular discretization is completely analogous to those for the even-parity equation with the exception that both $\vec{\Omega}$ and $\vec{\Omega}'$ are always in the angular domain. Thus, the parity-equivalent reflective boundary conditions are a little less complicated for the SAAI equation with S_n angular discretization.

A.5. SAAI non-essential reflective condition

The implementation of non-essential non-symmetric reflective boundary conditions for the SAAI S_n equations is extremely easy. In particular, on a reflective surface, the surface intensity in Eq. (A.3), ψ_s, is defined as follows:

$$\psi_s(\vec{\Omega}) = \tilde{\psi}(\vec{\Omega}') \quad \text{for } \vec{\Omega}\cdot\vec{n} < 0, \tag{A.35}$$

$$\psi_s(\vec{\Omega}) = \tilde{\psi}(\vec{\Omega}) \quad \text{for } \vec{\Omega}\cdot\vec{n} > 0. \tag{A.36}$$

Just as is the case for the first-order form of the transport equation, the incoming intensities depend upon the outgoing intensities, but the outgoing intensities do not depend upon the incoming intensities. This is obviously a non-symmetric coupling. However, as previously discussed, such coupling entails no penalty provided the standard S_n source iteration technique is used. In our opinion, the ease of implementing these reflective boundary conditions gives the SAAI S_n equations a significant advantage relative to the even-parity and odd-parity S_n equations.

References

[1] E.W. Lewis, W.F. Miller, Computational Methods of Neutron Transport, American Nuclear Society, Lagrange Park, IL, 1993.
[2] J.E. Morel, J.M. McGhee, A self-adjoint angular flux equation, Nucl. Sci. Eng. 12 (1998) 34.
[3] A. Kaplan, J.A. Davis, Canonical and involutory transformations of variational problems of transport theory, Nucl. Sci. Eng. 28 (1967) 166.
[4] H.G. Kaper, G.K. Leaf, A.J. Lindeman, Application of finite-element techniques for the numerical solution of neutron transport and diffusion equations, in: Proceedings of Second Conference on Transport Theory, Los Alamos Scientific Laboratory Report CONF-710107, 1971, p. 258.
[5] E.E. Lewis, Finite-element approximation to the even-parity transport equationAdv. Nucl. Sci. Technol., vol. 13, Plenum Press, New York, 1981, pp. 155–225.
[6] J.K. Fletcher, Solution of the multigroup neutron transport equation using spherical harmonics, Nucl. Sci. Eng. 84 (1983) 33.
[7] J.G. Issa, N.S. Riyait, A.J.H. Goddard, G.E. Stott, Multigroup application of the anisotropic FEM Code FEKTRAN to one, two, three-dimensions and R-Z problems, Prog. Nucl. Energ. 18 (1986) 251.
[8] C.R.E. de Oliveira, An arbitrary geometry finite-element method for multigroup neutron transport with anisotropic scattering, Prog. Nucl. Energ. 18 (1986) 227.
[9] C.R.E. de Oliveira, R.T. Ackroyd, A.J.H. Goddard, Finite-element treatment of non-linear thermal radiation transport, Trans. Am. Nucl. Soc. 68 (1993) 204.
[10] C.R.E. de Oliveira, C.C. Pain, A.J.H. Goddard, The finite-element method for time-dependent radiation transport applications, in: Proceedings of the 1998 Radiation Protection and Shielding Division Topical Conference, April 19–23, Nashville, TN, 1998.
[11] W.F. Miller, An analysis of the finite-differenced even-parity discrete-ordinates equations in slab geometry, Nucl. Sci. Eng. 108 (1991) 247.
[12] J.E. Morel, J.M. McGhee, A diffusion-synthetic acceleration technique for solving the even-parity S_n equations with anisotropic scattering, Nucl. Sci. Eng. 120 (1995) 147–164.
[13] R.T. Ackroyd, C.R.E. de Oliveira, A variational treatment for the time-dependent Boltzmann transport equation as a basis for numerical solutions conserving neutrons, Prog. Nucl. Energ. 30 (1996) 417.
[14] C.R. Drumm, J. Lorenz, Parallel FE electron–photon transport analysis on a 2-D unstructured mesh, in: Mathematics and Computation, Reactor Physics and Environmental Analysis in Nuclear Applications, Madrid, Spain, September, 1999.
[15] J. Liscum-Powell, A.K. Prinja, J.E. Morel, L.J. Lorence Jr., Nested acceleration algorithm for self-adjoint angular flux Boltzmann-CSD equation, Trans. Am. Nucl. Soc. 83 (2000) 253–254.

[16] C.R. Drum, J. Lorenz, Parallel FE approximation of the even–odd-parity form of the linear Boltzmann equation, Math. Comp. Model. 31 (2000) 55–71.
[17] O.C. Zienkiewicz, R.L. Taylor, fourth ed.The Finite-Element Method, vol. 1, McGraw-Hill Book Company, New York, 1994.
[18] R.T. Ackroyd, M.M. Nanneh, Hybrid principle with application to synthesis, Prog. Nucl. Energ. 25 (1991) 199–208.
[19] M.L. Adams, Even- and odd-parity finite-element transport solutions in the thick diffusion limit, in: Proceedings of the International Topical Meeting on Advances in Mathematics, Computations, and Reactor Physics, The American Nuclear Society, Pittsburgh, PA, 1991, pp. 21.1 (2-1 to 2-12).
[20] C.J. Gesh, M.L. Adams, Even- and odd-parity finite-element solutions to thick diffusive problems in cartesian geometry, in: Proceedings of the International Conference on Mathematics and Computation, Reactor Physics and Environmental Analysis in Nuclear Applications, The American Nuclear Society, Madrid, Spain, 1999, pp. 1175–1184.
[21] C.J. Gesh, M.L. Adams, Finite-element solutions of second-order forms of the transport equation at the interface between diffusive and non-diffusive regions, in: Proceedings ANS International Meeting on Mathematical Methods for Nuclear Applications: M&C 2001, The American Nuclear Society, Salt Lake City, UT, 2001, pp. 1–15.
[22] J.E. Morel, T.A. Wareing, K. Smith, A linear-discontinuous spatial differencing scheme for S_n radiative transfer calculations, J. Comput. Phys. 128 (1996) 445–462.
[23] T.J. Urbatsch, T.M. Evans, M. Buksas, Release Notification: MILAGRO-3_0_0: Multigroup, Research Note CCS-4:02-13(U), Los Alamos National Laboratory, LA-UR-02-3213, May 28, 1999.
[24] T.J. Urbatsch, T.M. Evans, M.W. Buksas, Milagro, Version 3.0, Los Alamos National Laboratory Computer Code, LA-CC-03-009, February, 2003.
[25] A.G. Petschek, R.E. Williamson, J.K. Wooten Jr., The Penetration of Radiation with Constant Driving Temperature, Technical Report LAMS-2421, Los Alamos Scientific Laboratory, July, 1960.
[26] P.F. Batcho, Private Communication, Los Alamos National Laboratory, December, 2003.
[27] B.T. Adams, J.E. Morel, T. Noh, J.M. McGhee, Experience with Self-Adjoint Forms of the Radiative Transfer Equations, Los Alamos National Laboratory Technical Report, LA-UR-04-9123, January, 2005.